AD-A082 190 SRI INTERNATIONAL MENLO PARK CA F/G 20/14
THE TEMPORAL STRUCTURE OF STRONGLY SCINTILLATING SIGNALS.(U)
JAN 79 C L RINO, J OWEN DNA001-77-C-0220
UNCLASSIFIED DNA-4827T NL

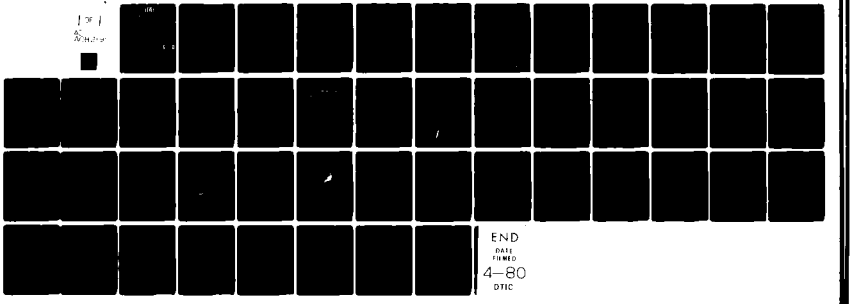

END
DATE FILMED
4-80
DTIC

(12) LEVEL III

DNA 4827T

THE TEMPORAL STRUCTURE OF STRONGLY SCINTILLATING SIGNALS

SRI International
333 Ravenswood Avenue
Menlo Park, California 94025

31 January 1979

Topical Report for Period 1 August 1978—31 December 1978

CONTRACT No. DNA 001-77-C-0220

THIS WORK SPONSORED BY THE DEFENSE NUCLEAR AGENCY
UNDER RDT&E RMSS CODE B322078462 I25AAXHX63340 H2590D.

Prepared for
Director
DEFENSE NUCLEAR AGENCY
Washington, D. C. 20305

Destroy this report when it is no longer needed. Do not return to sender.

PLEASE NOTIFY THE DEFENSE NUCLEAR AGENCY, ATTN: STTI, WASHINGTON, D.C. 20305, IF YOUR ADDRESS IS INCORRECT, IF YOU WISH TO BE DELETED FROM THE DISTRIBUTION LIST, OR IF THE ADDRESSEE IS NO LONGER EMPLOYED BY YOUR ORGANIZATION.

UNCLASSIFIED

SECURITY CLASSIFICATION OF THIS PAGE *(When Data Entered)*

REPORT DOCUMENTATION PAGE		READ INSTRUCTIONS BEFORE COMPLETING FORM
1. REPORT NUMBER DNA 4827T	2. GOVT ACCESSION NO.	3. RECIPIENT'S CATALOG NUMBER
4. TITLE *(and Subtitle)* THE TEMPORAL STRUCTURE OF STRONGLY SCINTILLATING SIGNALS		5. TYPE OF REPORT & PERIOD COVERED Topical Report for Period 1 Aug 78—31 Dec 78
		6. PERFORMING ORG. REPORT NUMBER SRI Project 6434
7. AUTHOR(s) Charles L. Rino Jacqueline Owen		8. CONTRACT OR GRANT NUMBER(s) DNA 001-77-C-0220
9. PERFORMING ORGANIZATION NAME AND ADDRESS SRI International 333 Ravenswood Avenue Menlo Park, California 94025		10. PROGRAM ELEMENT, PROJECT, TASK AREA & WORK UNIT NUMBERS Subtask I25AAXHX633-40
11. CONTROLLING OFFICE NAME AND ADDRESS Director Defense Nuclear Agency Washington, D.C. 20305		12. REPORT DATE 31 January 1979 13. NUMBER OF PAGES 50
14. MONITORING AGENCY NAME & ADDRESS(if different from Controlling Office)		15. SECURITY CLASS (of this report) UNCLASSIFIED 15a. DECLASSIFICATION DOWNGRADING SCHEDULE

16. DISTRIBUTION STATEMENT *(of this Report)*

Approved for public release; distribution unlimited.

17. DISTRIBUTION STATEMENT *(of the abstract entered in Block 20, if different from Report)*

18. SUPPLEMENTARY NOTES

This work sponsored by the Defense Nuclear Agency under RDT&E RMSS Code B322078462 I25AAXHX63340 H2590D.

19. KEY WORDS *(Continue on reverse side if necessary and identify by block number)*

Scintillation
Propagation
Strong Scattering

20. ABSTRACT *(Continue on reverse side if necessary and identify by block number)*

This report describes a detailed analysis of the time structure of scintillation signals based on Wideband satellite equatorial scintillation data recorded at Kwajalein and at Ancon, Peru. The results verify theoretically derived upper and lower bounds on the fade coherence time that are currently being used for system studies. Under conditions of strong scattering, the theory is surprisingly accurate. The data also show subtle structural differences between the Ancon and Kwajalein data that are attributed to slight differences in the power-law spectral indices at the two stations.

DD FORM 1 JAN 73 1473 EDITION OF 1 NOV 65 IS OBSOLETE

UNCLASSIFIED

SECURITY CLASSIFICATION OF THIS PAGE *(When Data Entered)*

EXECUTIVE SUMMARY

This report describes the results of a detailed study of the temporal fading structure of scintillating signals, particularly under conditions of strong scattering. In a slow-fading environment, the single-bit error rate depends only on the probability density of the signal fades; but the fade coherence time, τ_I, ultimately determines the impact of errors in a data stream and the effectiveness (cost) of various coding schemes for preserving message integrity. In a pure Rayleigh fading environment the scintillation index is unity, and the coherence time of the complex signal, which is simply related to τ_I, essentially determines the environmental limitations to the performance of any coherent or noncoherent signaling scheme. Coherence bandwidth effects will be discussed in a separate report.

The principal result of this study is the verification of the lower and upper bounds for τ_I that are coming into increasing use for system performance evaluation. Under conditions of weak scattering, τ_I is a monotonic function of the Fresnel radius divided by the effective scan velocity $\sqrt{z}/v_{eff}$. The details of the functional dependence of τ_I on $\sqrt{z}/v_{eff}$ depend on the power-law index of the irregularity (or phase) spectral density function. In general, however, $\tau_I < \sqrt{z}/v_{eff}$.

From the Wideband data presented in this report we find clear evidence of the effects of a varying spectral index. The wavelength dependence of τ_I as determined from Wideband data recorded at Ancon is significantly different from that determined from data recorded at Kwajalein. This difference is consistent with the measured phase spectral indices (Rino and Matthews, 1978) and frequency dependences of S_4 (Livingston, 1978) at the two stations.

In spite of these subtleties, the data do verify that $\tau_I < \sqrt{z}/v_{eff}$. The bound is rather crude, but adequate for most engineering purposes. Indeed, under conditions of weak scattering, performance degradation is

generally not severe. If a tighter bound is warranted, it can be obtained by performing appropriate numerical integrations.

Under conditions of sufficiently strong scattering, the fading statistics are well approximated by the Rayleigh model. In that case the structure of the signal intensity can be characterized by a simple asymptotic limiting form of the intensity correlation function. Detailed analysis presented in Rino (1978) shows that for a phase spectral density function of the form f^{-p}, $\tau_I \propto T^{1/(p-1)}$. This result is strictly valid only for $1 < p < 3$. No simple asymptotic bound exists for $p \geq 3$. To summarize, as one progresses from weak to strong scattering, τ_I changes from Fresnel radius control, $\tau_I < \sqrt{Z}/v_{eff}$, to perturbation strength control, $\tau_I \propto T^{1/(p-1)}$. This transition is clearly evident in the Wideband data.

However, a significant and unexpected result is that under conditions of strong scattering there is virtually a unique one-to-one relation between τ_I and T. That is, there is surprisingly little dispersion in a plot of τ_I vs T. The asymptotic formula for the intensity correlation function gives a tight lower bound for τ_I, provided that p lies in the range of measured p values, $2.3 \leq p \leq 2.5$. Since the calculated values of τ_I decrease with increasing p, using p values near 3 causes the measured τ_I value to be severely underestimated.

Overall, the results of our analysis further demonstrate the utility of the phase screen model for calculating propagation effects. The phase spectral strength parameter T contains all the necessary spatial-to-temporal conversions and the geometrical effects of propagation through highly anisotropic media. It must be kept in mind, however, that the phase screen parameters are spatial averages over the entire propagation path. The ramifications of this fact are discussed in Section V.

The data used in this study were processed with both a longer detrend interval (25 s) and a higher sample rate (250 Hz) than are used in the routine summary processing of the Wideband data. This provided an opportunity to double-check the results of our routine data analysis.

The analysis does confirm that the spectral slopes are generally less than 3, and that there is a systematic difference between the Ancon and Kwajalein data, with the latter showing somewhat shallower spectral slopes. Also, the longer detrend intervals increased the measured S_4 values under strong-scatter conditions. This was anticipated, based on the data analysis reported in Rino and Matthews (1978).

For completeness, the phase scintillation was also analyzed. The simple linear dependence of the rms phase is a good approximation to the median behavior of phase scintillation for all perturbation levels. That is, there is no saturation of the phase scintillation as there is with intensity. However, the dispersion about the mean increases steadily with increasing perturbation levels. The diffraction effects in the phase data are evidently behaving somewhat like additive noise.

Finally, for engineering applications, we have computed the average mean signal level crossing time, which is easily measured, and compared it with the time delay to 50% intensity decorrelation, which is our definition of τ_I. As one should expect, the two coherence time measures are simply proportional, particularly under strong-scatter conditions.

CONTENTS

ILLUSTRATIONS

I INTRODUCTION AND BACKGROUND

Equatorial gigahertz scintillation is one of a variety of phenomena that are now collectively referred to as "equatorial spread-F." The discovery of gigahertz scintillation (Craft and Westerlund, 1972) was unexpected, although nighttime equatorial scintillation has been studied for a number of years prior to Craft and Westerlund's discovery (Koster, 1968, 1972).

The scintillation of transionospheric radio signals can degrade the performance of satellite communication links. Thus, practical considerations have motivated a large research effort over the years. More recently, the discovery of ionospheric electron density depletions (Kelley et al., 1976) and their association with equatorial three-meter backscatter (Woodman and La Hoz, 1976) have directed the attention of researchers to physical processes that can explain the development of the very intense irregularities that cause gigahertz scintillation (Ossakow and Chaturvedi, 1978; Ott, 1978).

With regard to the structure of the ionospheric irregularities that cause the scintillation effects, it is now known that they encompass a large continuum of scale sizes that can be characterized by a power-law spectral density function (SDF). When the Fresnel radius lies within the range of scale sizes characterized by the power-law continuum, the scintillation theory for both weak and strong scattering admits a simple formulation. The weak-scatter theory is described in Rino and Matthews (1978). The extension of the theory to strong scattering is described in Rino (1978) and the references cited therein.

In this report we present equatorial data from the Wideband satellite that verify the extension of the weak-scatter theory to strong scattering. The results are of immediate practical interest because they characterize the time structure of severely fading signals, which is crucial in evaluating system performance and designing effective

mitigants. Equally important, they provide a check on the measured and derived parameters that characterize the large body of Wideband satellite equatorial scintillation data that have been accumulated over the past two years.

Before presenting the data, however, we shall briefly review the principal theoretical results. For a power-law irregularity SDF of the form

$$\Phi_{\Delta N_e}(\kappa, \kappa_z) = C_s q^{-(2\nu+1)} \quad , \tag{1}$$

the S_4 scintillation index [$S_4 = (\langle I^2 \rangle - \langle I \rangle^2)^{1/2}/\langle I \rangle$] under conditions of weak scattering can be computed by using the formula

$$S_4^2 = r_e^2 \lambda^2 (L \sec \theta) C_s Z^{\nu-\frac{1}{2}} \left[\frac{\Gamma\left(\frac{2.5-\nu}{2}\right)}{2\sqrt{\pi}\,\Gamma\left(\frac{\nu+0.5}{2}\right)(\nu-0.5)} \right] \mathfrak{F} \tag{2}$$

where

$$Z = \frac{\lambda z \sec \vartheta}{4\pi} \tag{3}$$

and $\mathfrak{F}$ is a geometry-dependent propagation factor [see Rino and Matthews 1978, Eq. (31)]. For isotropic irregularities, $\mathfrak{F} = 1$; for highly elongated irregularities at near normal incidence, $\mathfrak{F} \approx \Gamma(\nu)/[\sqrt{\pi}\,\Gamma(\nu+\frac{1}{2})]$. In Eq. (2) r_e is the classical electron radius, λ is the wavelength, L is the layer thickness, θ is the zenith angle, and Z is the Fresnel radius. In Eq. (3), z_R is the reduced distance to the equivalent phase screen.

The average structure of the ionospheric irregularities is characterized by the strength of turbulence, C_s, and the spectral index parameter, ν. In the diffraction theory, the admissible range of ν values is $0.5 < \nu < 2.5$. If $\nu \geq 2.5$, an outer-scale cutoff must be introduced to avoid divergent integrals. Similarly, if $\nu \leq 0.5$, the inner-scale cutoff must be introduced. We note here that Costa and

Kelly (1976) have derived a formula that retains an explicit dependence on the outer scale when $\nu = 1.5$. For $\nu = 1.5$, Eq. (2) agrees with the Costa-Kelly result in the limit as the outer-scale wavenumber approaches zero.

In Figure 1, which is reproduced from Rino and Matthews (1978), we show some computations based on Eq. (2) for an overhead equatorial geometry at 1 GHz. The parameter a is the irregularity axial ratio. For $a \geq 10$ there is no change in S_4, and the propagation effects are essentially one-dimensional. It can be seen that for a 200-km layer at an altitude of 350 km, $C_s > 10^{20}$ in mks units is required to produce significant gigahertz scintillation.

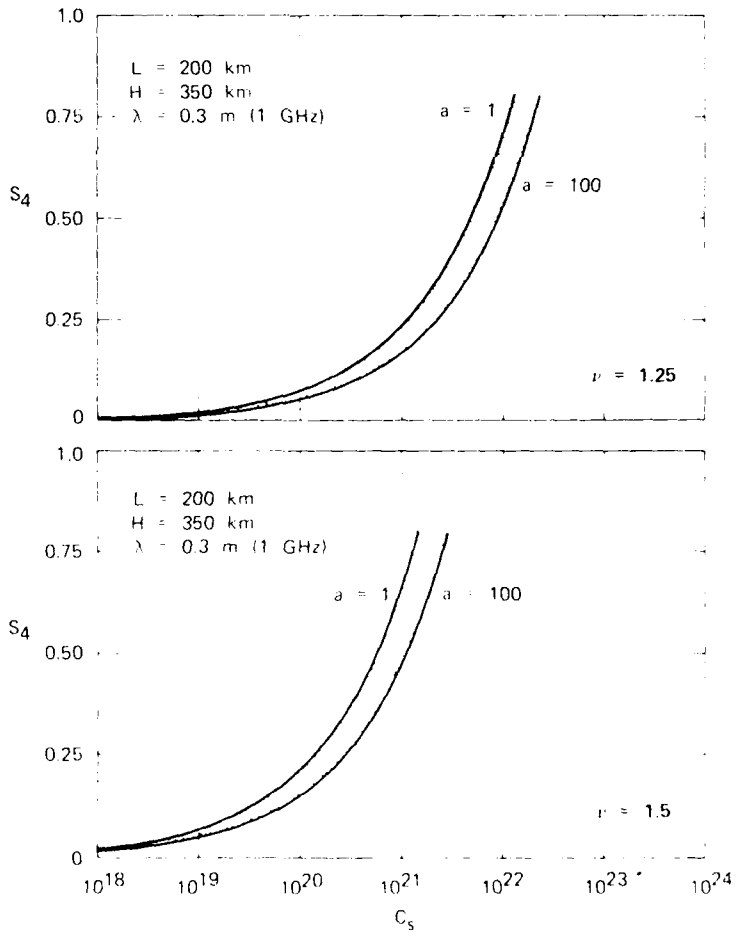

FIGURE 1 CALCULATED GIGAHERTZ SCINTILLATION FOR IDEALIZED EQUATORIAL GEOMETRY

The strength of turbulence is formally related to the rms electron density, $\langle \Delta N_e^2 \rangle^{\frac{1}{2}}$, and the outer-scale wavenumber, q_o, by the normalization relation

$$C_s = 8\pi^{3/2} \langle \Delta N_e^2 \rangle \, q_o^{2\nu-2} \, \Gamma(\nu+\tfrac{1}{2})/\Gamma(\nu-1) \quad . \tag{4}$$

In Figure 2, which is also from Rino and Matthews (1978), the rms electron density vs C_s for various $\ell_o = (2\pi/q_o)$ values has been plotted. The rms electron density values should be interpreted as what would be measured by an in-situ probe scanning along a path of length ℓ_o, since in most practical situations the path length is smaller than the outer-scale cutoff.

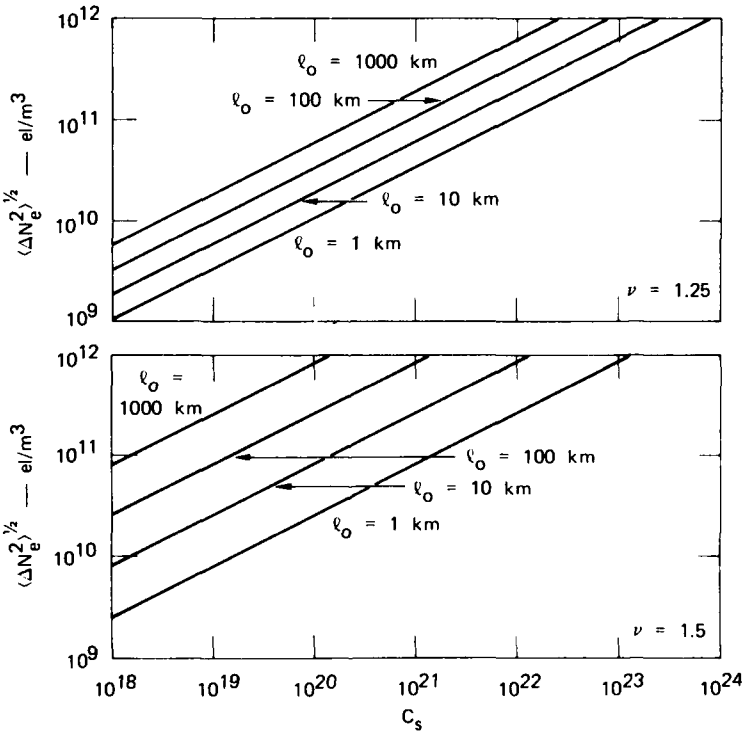

FIGURE 2 RMS ELECTRON DENSITY VARIATION vs. STRENGTH OF TURBULENCE FOR DIFFERENT VALUES OF ℓ_o

In any case, it can readily be seen that the perturbation levels required to produce gigahertz scintillation are very large indeed. It should be kept in mind, however, that insofar as the scintillation theory is concerned, C_s and ν are effective parameters that result from an average over the entire propagation path. Thus, the detailed relationship between C_s, ν, and the corresponding in-situ parameters remains to be demonstrated.

Moreover, to fully characterize the data, we must take into account that only time-varying signals are actually measured. For a low-orbiting satellite such as Wideband, the temporal-to-spatial conversion is critically dependent upon the propagation geometry. Under weak-scatter conditions, the temporal SDF of the phase scintillation has the power-law form

$$\varphi(f) = Tf^{-p} \tag{5}$$

where

$$p = 2\nu \tag{6}$$

As discussed in Fremouw et al. (1978), the parameters T and p are routinely measured in the Wideband data analysis. The relationship between C_s and T [Rino and Matthews, 1978], is

$$T = r_e^2 \lambda^2 \, (L \sec \theta) \, C_s G \, \frac{\sqrt{\pi}\,\Gamma(\nu)}{(2\pi)^{2\nu+1}\,\Gamma(\nu+\frac{1}{2})} \, v_{eff}^{2\nu-1} \tag{7}$$

where both G and v_{eff} depend on the propagation geometry.

The parameter G accounts for the scintillation enhancement as the propagation vector intercepts the principal irregularity axes, both along and (if appropriate) across the magnetic field direction. The parameter, v_{eff}, which has the units of velocity, gives the temporal-to-spatial coordinate conversion--i.e., $\kappa = (2\pi f/v_{eff})$. For isotropic irregularities or cross-field scan directions, $v_{eff} = v_\perp$, where $v_\perp$ is the component of the scan velocity perpendicular to the propagation direction. In general, $v_{eff} \leq v_\perp$.

As C_s increases, the measured value of S_4 ultimately falls below that predicted by Eq. (2). Numerical calculations for a strict power-law environment predict S_4 values increasing to a maximum value somewhat larger than unity and then converging to unity from above [Rumsey (1975); Marians (1975)]. For Rayleigh fading, $S_4 = 1$, although $S_4 = 1$ is not a sufficient condition to guarantee Rayleigh fading. When $S_4 > 1$, there is an excess of signal enhancements over that expected for pure Rayleigh fading. The degree to which this effect occurs, depends on the spectral index ν. Spectra with large ν values intensify the scale-size regime near the Fresnel frequency, which produces so called strong focusing. When this occurs, the S_4 index exceeds unity.

Pure Rayleigh fading, however, is the most commonly used engineering model. If x and y are zero-mean and uncorrelated but identical Gaussian processes, then the complex signal $v = x + iy$ has a Rayleigh distribution for its intensity, I, ($I = |v|^2$) and a uniformly distributed phase between 0 and 2π radians. The quantity $\langle vv'^* \rangle$ is called the mutual-coherence function, and the relation

$$\langle II' \rangle - \langle I \rangle^2 = |\langle vv'^* \rangle|^2 = 4\langle xx' \rangle^2 \tag{8}$$

is easily verified. Since $\langle I \rangle = 2\langle x^2 \rangle = 1$, it follows from the definition of S_4 and Eq. (8) that $S_4 = 1$ as noted above.

It is also well known (Fejer, 1953; Bramley, 1954) that for a multiply scattered wavefield in a uniform medium,

$$\langle vv'^* \rangle = \exp\left\{-\tfrac{1}{2} D(\vec{\Delta\rho})\right\} \tag{9}$$

where $D(\vec{\Delta\rho})$ is the phase structure function

$$D(\Delta\rho) = \langle (\delta\phi - \delta\phi')^2 \rangle \quad , \tag{10}$$

and

$$\delta\phi = r_e \lambda \int \Delta N_e \, d\ell \quad . \tag{11}$$

The integral is evaluated along the propagation path. Thus, under conditions of sufficiently strong scattering where $S_4 \sim 1$ and a relationship such as Eq. (8) is expected to hold, Eq. (9) can be used to derive a simple asymptotic expression for the fade coherence time.

In Rino (1978) a detailed analysis of the intensity correlation function under conditions of strong scattering is presented. The analysis shows that in a strict power-law environment, the asymptotic strong-scatter limit, Eq. (8), is valid as long as $\nu < 1.5$. If $\nu > 1.5$, $D(\vec{r})$ does not exist in the limit of an arbitrarily large outer scale, and the intensity correlation function as well as the mutual-coherence function retain dependences on the Fresnel radius no matter how strong the perturbation becomes. This is not a contradiction to the Fejer-Bramley result because a scattering medium with an arbitrarily large outer-scale parameter is not strictly uniform.

Nonetheless, in the simple case where $\nu < 1.5$, the time structure of the fading under strong-scatter conditions asymptotically approaches

$$\langle II' \rangle = \exp\left\{-D(\vec{v}_s \delta t)\right\} \quad . \tag{12}$$

It is shown in Rino (1978) that

$$D(v_s \delta t) = T\left[\frac{4\pi^{2\nu-0.5}\,\Gamma(1.5-\nu)}{(2\nu-1)\,\Gamma(\nu)}\right]|\delta t|^{2\nu-1} \quad . \tag{13}$$

Thus, the intensity coherence time under conditions of strong scattering admits a simple characterization that can be used to verify the measured T and $\nu = p/2$ values. We shall see that the results are in good agreement with the Wideband satellite data.

II THE DATA BASE

To obtain a representative data base of intense scintillation, we have selected sets of the most severely disturbed passes recorded at the Ancon (11°46'S, 77°09'W) and Kwajalein (9°24'N, 167°28'E) tracking stations. The specific passes are listed in the Appendix. The occurrence statistics of equatorial scintillation are discussed in Livingston (1978).

In the routine summary processing that is applied to all the Wideband satellite data, a 10-s detrend filter is used with a 100-Hz sample rate (Fremouw et al., 1978). To fully accommodate the spectral broadening associated with intense scintillation, however, it is desirable to increase the temporal resolution. Moreover, as discussed in Section IV of Rino and Matthews (1978), the 10-s detrend interval is evidently too short to fully accommodate the low-frequency content of the most severe equatorial intensity scintillation.

For this study, therefore, the L-band, center UHF, and VHF channels have been reprocessed at a 250-Hz sample rate using a 25-s detrend filter. The phase data were then spectrally analyzed to extract the T and p parameters [see Eq. (5)] as described in Fremouw et al. (1978). To characterize the time structure of the signal, the time lag to 50% intensity decorrelation was measured as well as the mean intensity crossing rate. The summary parameters were measured on non-overlapping 16-s time intervals.

To illustrate the effects of the detrender cutoff, in Figure 3 a segment of UHF data processed using both the standard 10-s detrend filter and a 25-s detrend filter is shown. To the eye, the intensity data are identical. Thus, there is very little spectral content in the intensity data below 0.1 Hz. This intrinsic high-pass structure of the intensity scintillation is caused by the diffraction process, which strongly suppresses Fourier modes with spatial periods longer than the Fresnel radius.

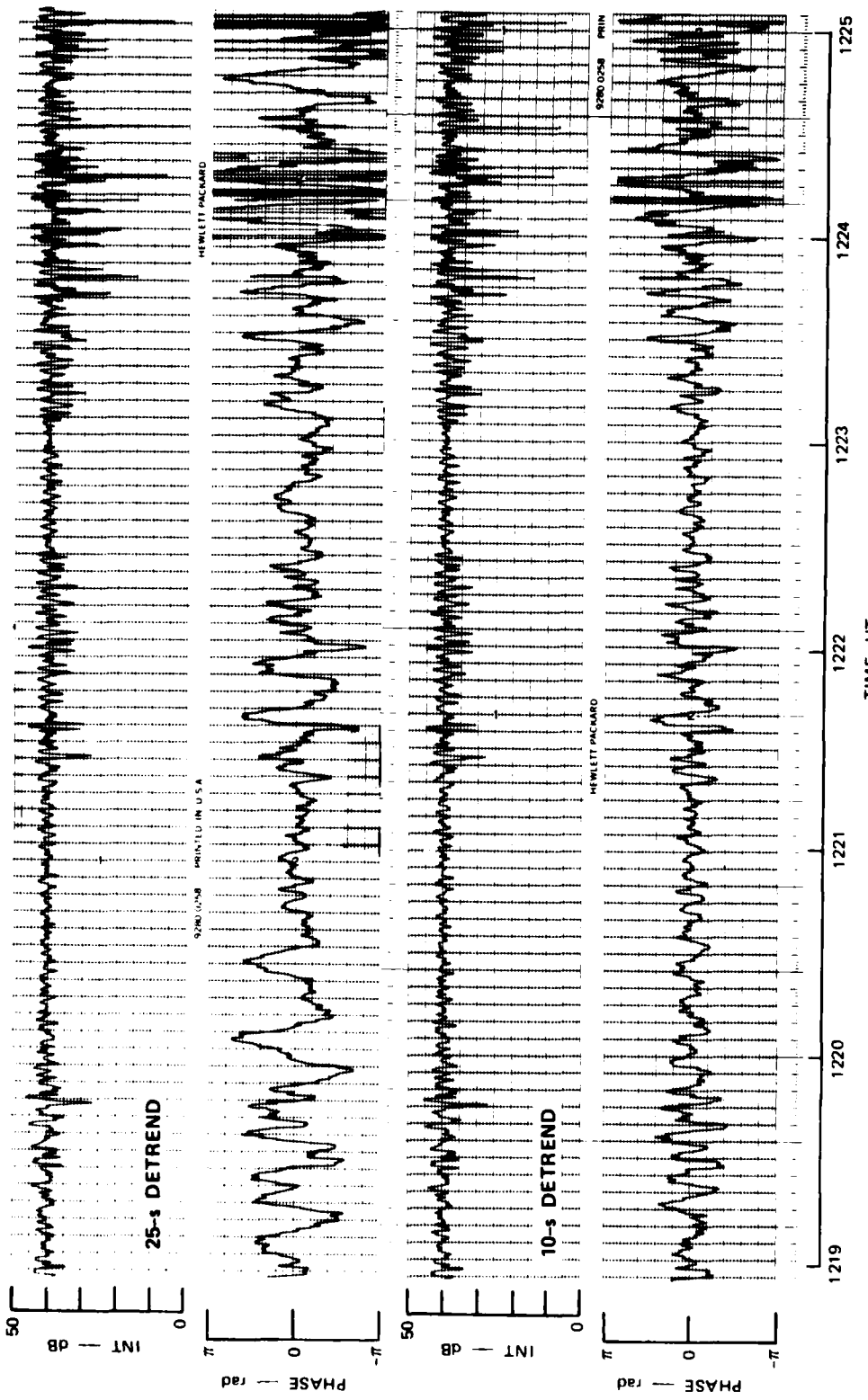

FIGURE 3 DATA SEGMENT SHOWING EFFECTS OF CHANGING DETREND FILTER CUTOFF

Since the phase data essentially map the integrated electron content along the propagation path, however, the low-frequency modes, which are the most intense in a power-law environment, dominate the phase structure. Thus, there is a dramatic increase in the low-frequency content of the phase scintillation data when the detrend interval is increased.

This intrinsic nonstationarity in the phase data is easily characterized in terms of the T and p parameters. For example, the measured phase variance is

$$\langle \delta\phi^2 \rangle = 2T \int_{\tau_c^{-1}}^{\infty} f^{-p}\, df$$

$$= \frac{2T}{p-1}\, \tau_c^{p-1} \qquad (14)$$

where τ_c is the detrend interval. The Wiener process, which is used to model Brownian motion, has a similar property [Uhlenbeck and Ornstein, 1930].

Unfortunately, there is no theory that either adequately accommodates diffraction effects in phase scintillation or even addressed the phase structure under conditions of strong scattering. In our analysis, only the zeroth-order approximation, under which diffraction effects are entirely neglected, has been considered. Thus, the temporal phase SDF has the form Tf^{-p}; p is independent of wavelength and T varies quadratically with wavelength.

It follows from Eq. (14) that

$$\sigma_\phi = \langle \delta\phi^2 \rangle^{1/2} \propto \lambda \quad . \qquad (15)$$

To correct for a finite reference frequency, Eq. (15) must be multiplied by $1 - (f/f_r)^2$, where $f = c/\lambda$, and f_r is the reference frequency. Thus, the wavelength dependence of the rms phase gives one simple test of the adequacy of the simplest theory. In Figure 4 we show scatter diagrams of

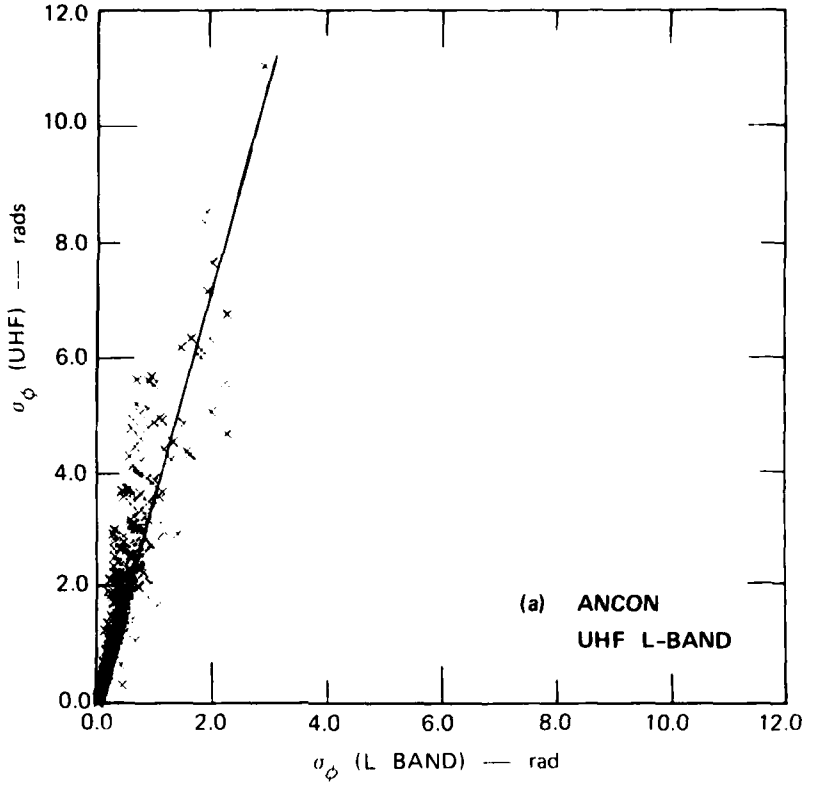

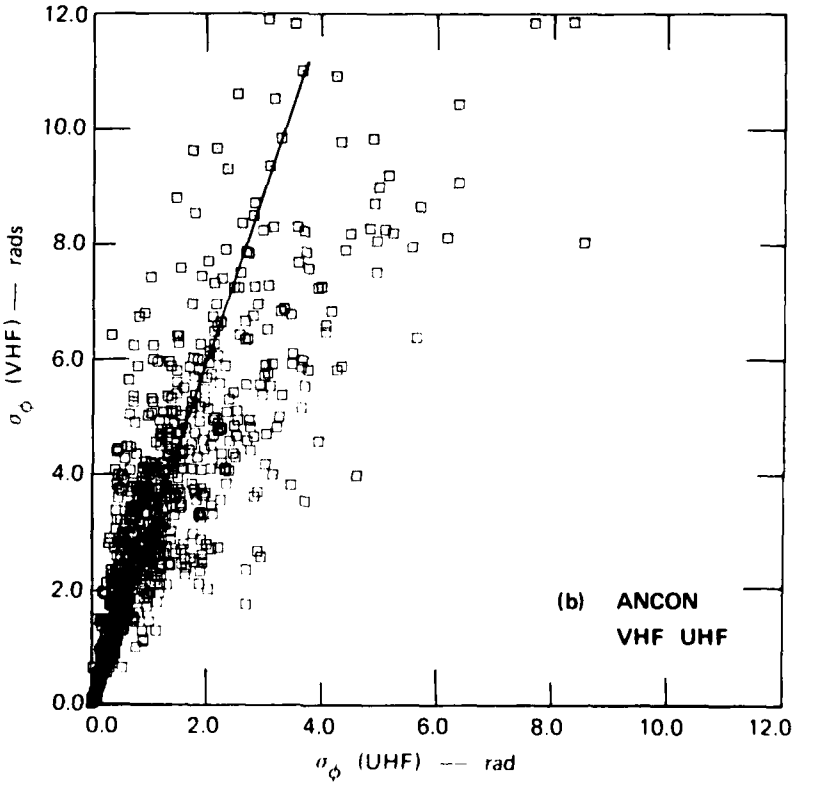

FIGURE 4 SCATTER PLOTS OF σ_ϕ FOR ANCON DATA

rms phase for L-band vs UHF and UHF vs VHF from the Ancon data. The corresponding scatter diagrams for the Kwajalein data are shown in Figure 5.

When the rms phase is less than a few radians, the data adhere very closely to the theoretical curves. For larger perturbation levels there is steadily increasing but essentially uniform scatter about the theoretically predicted means. There is evidently no saturation effect as there is with the S_4 intensity scintillation index.

Intuitively, it is clear that diffraction-induced departures from the simple theory are caused by the rapid phase changes that accompany deep fades. Thus, it is mainly the high frequencies that are affected, and the increasing scatter in Figures 4 and 5 for the larger perturbations is essentially additive "diffraction" noise.

It should be kept in mind that there is no significance to the absolute rms phase. From Eq. (14), however, for p = 3, $\langle \delta\phi^2 \rangle = T\tau_c^2$. Thus, the one radian level where diffraction effects become significant corresponds to $T = 1.6 \times 10^{-3}$, or -28 dB. It is convenient to express T in dB because it is numerically equal to the phase SDF evaluated at 1 Hz.

In Figures 6 and 7 the averages of the measured p indices are shown for the Ancon and Kwajalein data sets, respectively. The data have been ordered by scintillation level to show any systematic changes with perturbation strength. For very weak scintillation ($S_4 \leq 0.1$) the system noise obscures the phase SDF and p is artificially decreased. For large perturbation levels ($S_4 \gtrsim 0.8$), diffraction effects act to reduce the phase-spectral slope.

The shaded regions in Figure 6 denote the standard deviation of the UHF data. The data in Figures 6 and 7 show that for comparable perturbation levels, the measured p indices are indeed wavelength-invariant. Moreover, the median p values for the intermediate S_4 range where neither noise contamination nor diffraction significantly affect the measurements, are consistently lower than p = 3. Finally, we note that there is a small but systematic difference between the spectral slopes from the Ancon data and the Kwajalein data. For the former, $\bar{p} \sim 2.6$, and $\bar{p} \sim 2.4$ for the latter.

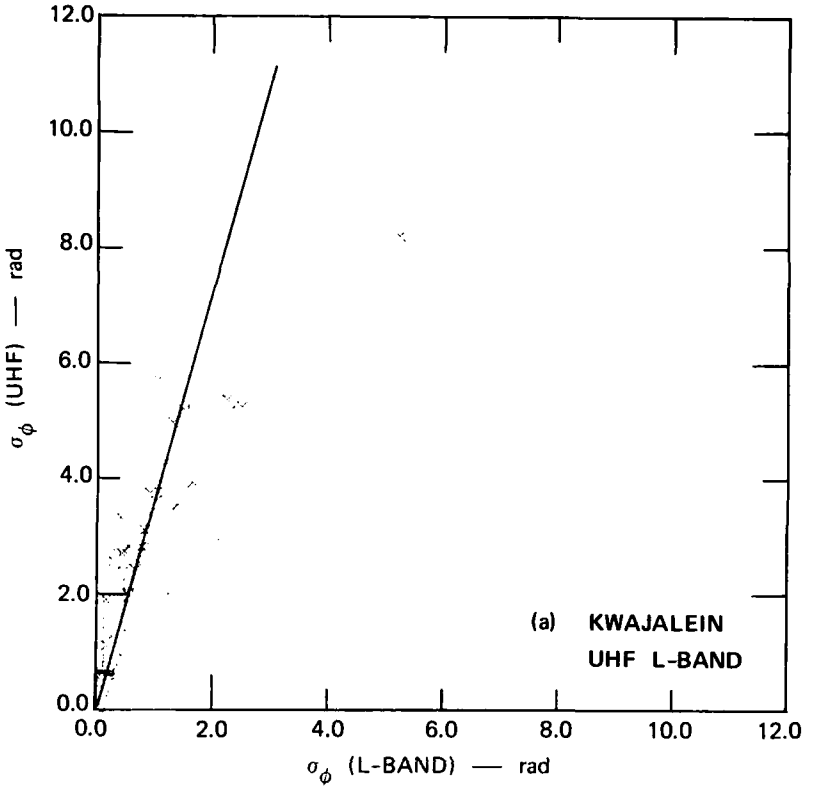

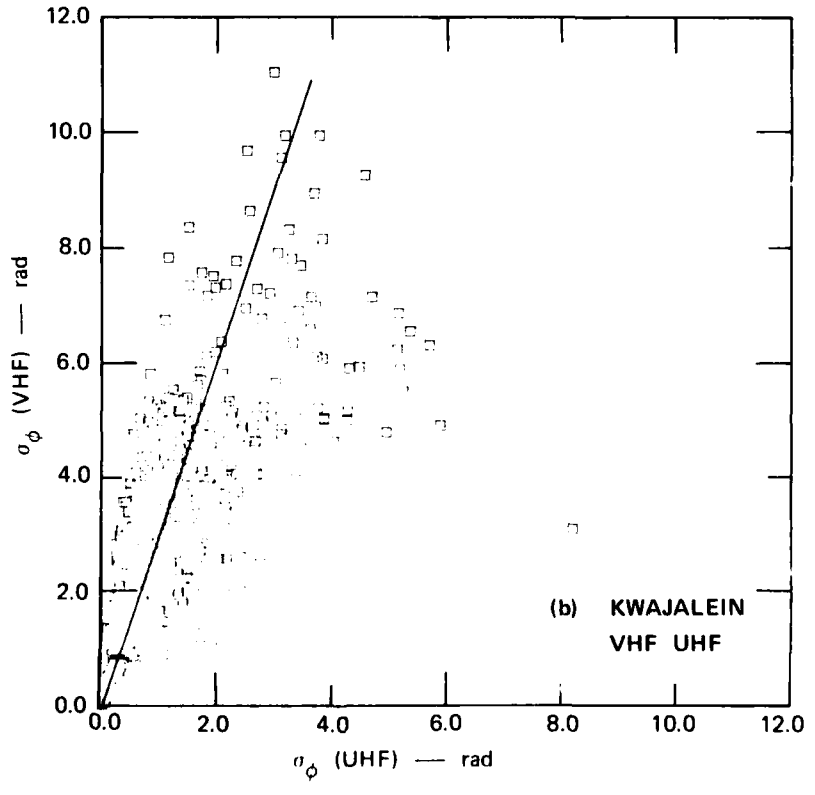

FIGURE 5 SCATTER PLOTS OF σ_ϕ FOR KWAJALEIN DATA

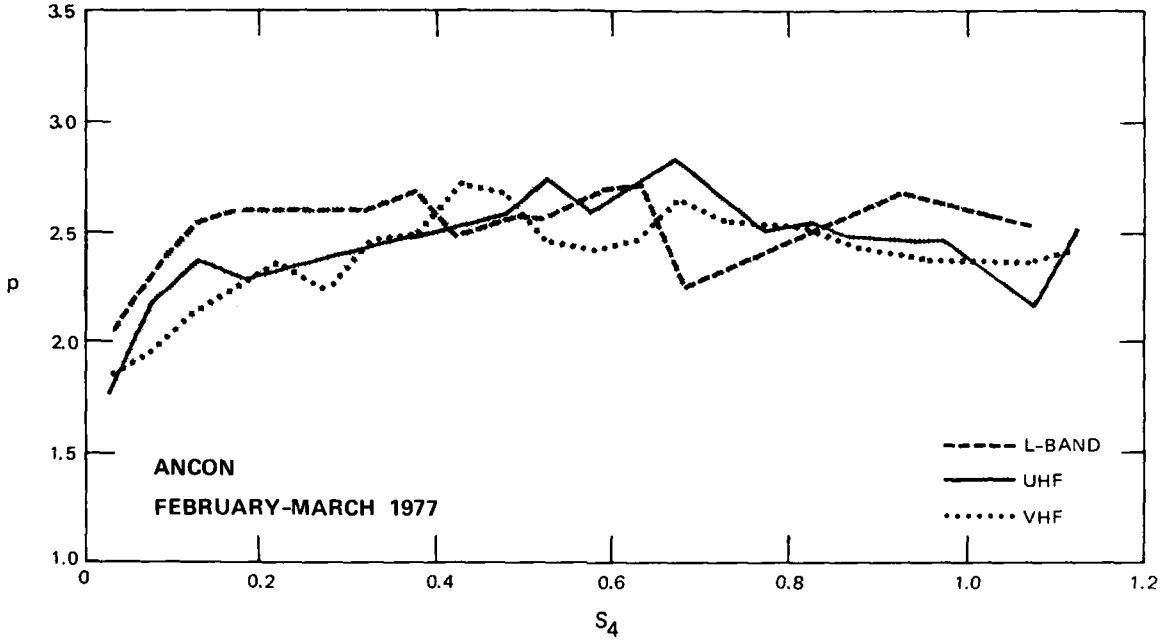

FIGURE 6 AVERAGE OF MEASURED ANCON p INDICES AT VHF, UHF, AND L-BAND PLOTTED AGAINST S_4

The results confirm the earlier findings reported in Rino and Matthews (1978) that were based on the standard summary data. Moreover, Livingston (1978) reports a difference in the wavelength dependence of the average intensity scintillation measured at Ancon and Kwajalein. For roughly comparable L-band scintillation levels, there is significantly more VHF scintillation observed at Ancon than at Kwajalein. This difference can be fully accounted for by the slight difference in spectral slopes, with the steeper-slope spectra producing more intensity scintillation for the same perturbation level (see Figure 1).

Turning now to the intensity scintillation, in Figures 8 and 9 the two-frequency scatter diagrams of measured S_4 values that correspond to Figures 4 and 5, respectively, are shown. Under conditions of weak scatter (say $S_4 \leq 0.4$) there is a sensibly linear relation between the S_4 values measured at two different frequencies. This is in agreement with the weak-scatter theory, which predicts

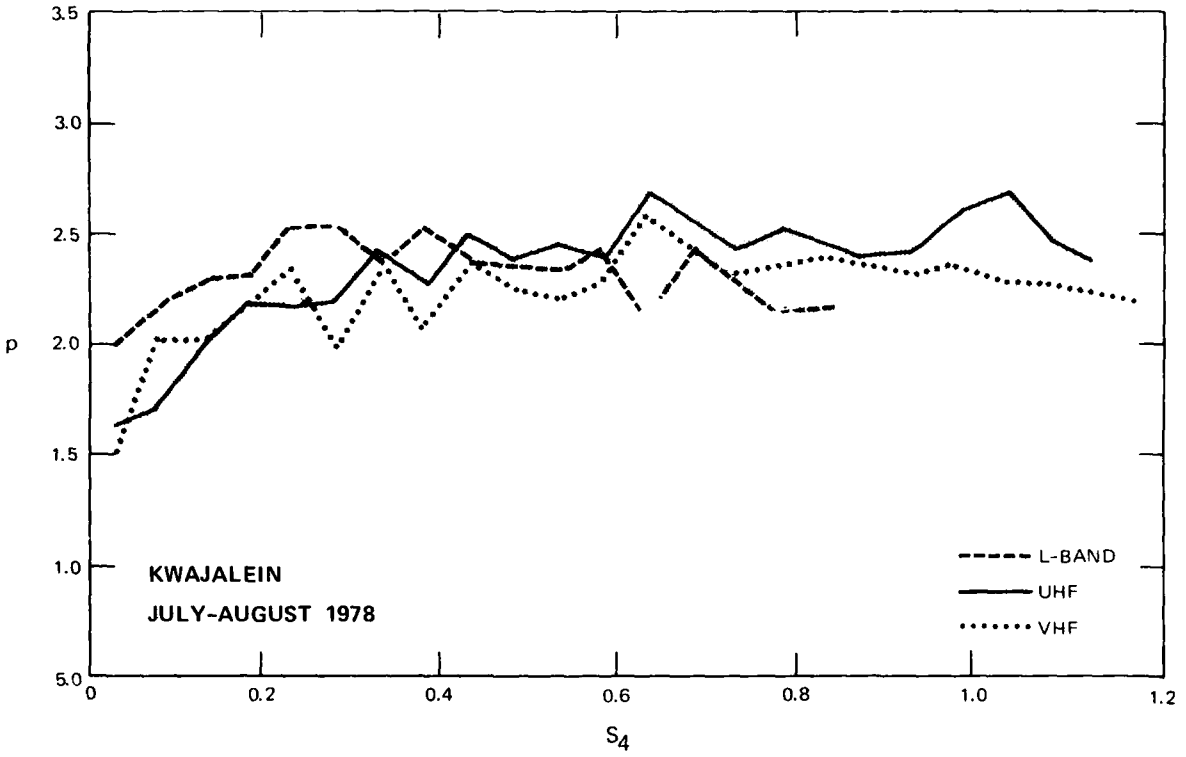

FIGURE 7 AVERAGE OF MEASURED KWAJALEIN p INDICES AT VHF, UHF, AND L-BAND PLOTTED AGAINST S_4

$$S_4 \propto \lambda^{\frac{p+3}{4}} \tag{16}$$

[see Eq. (2) and recall that $p = 2\nu$].

Unfortunately, the scatter in the measured data points is such that the departure of the spectral slopes from p = 3 and the subtle differences between Ancon and Kwajalein are not immediately apparent. On the other hand, if Figures 8(a) and 9(a) are compared, it can be seen that there are relatively fewer Kwajalein data points in the intermediate S_4 range. As discussed in Livingston (1978), this effect is consistent with the small difference in spectral slopes.

Under strong-scatter conditions there is essentially uniform scatter about $S_4 = 1$. We believe that these are statistical fluctuations rather than evidence of the strong focusing effect discussed in Section I. Indeed, in a one-dimensional medium the strong focusing effect does not

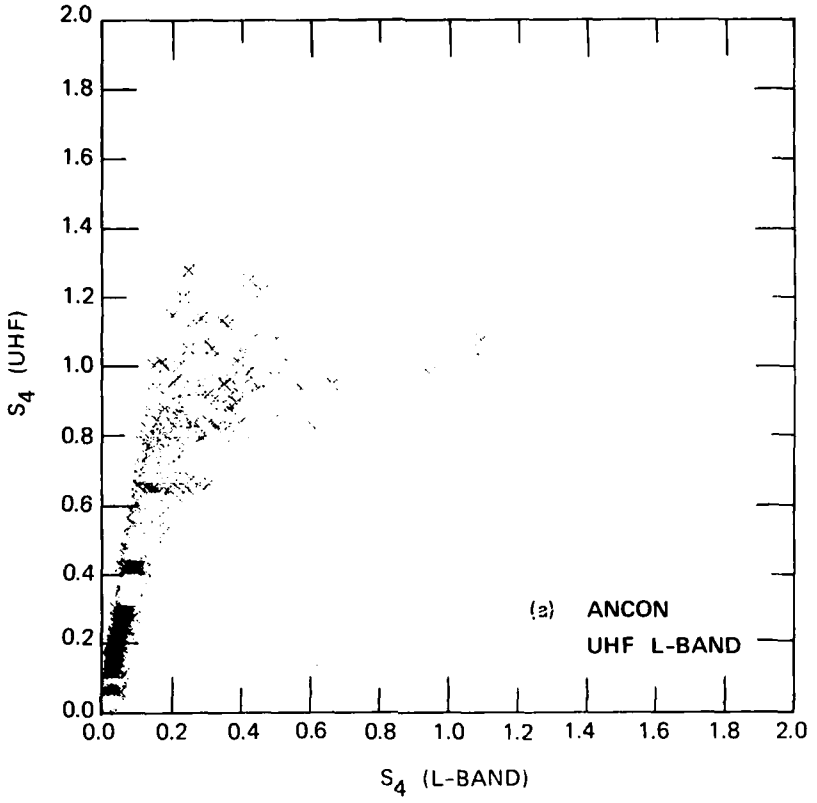

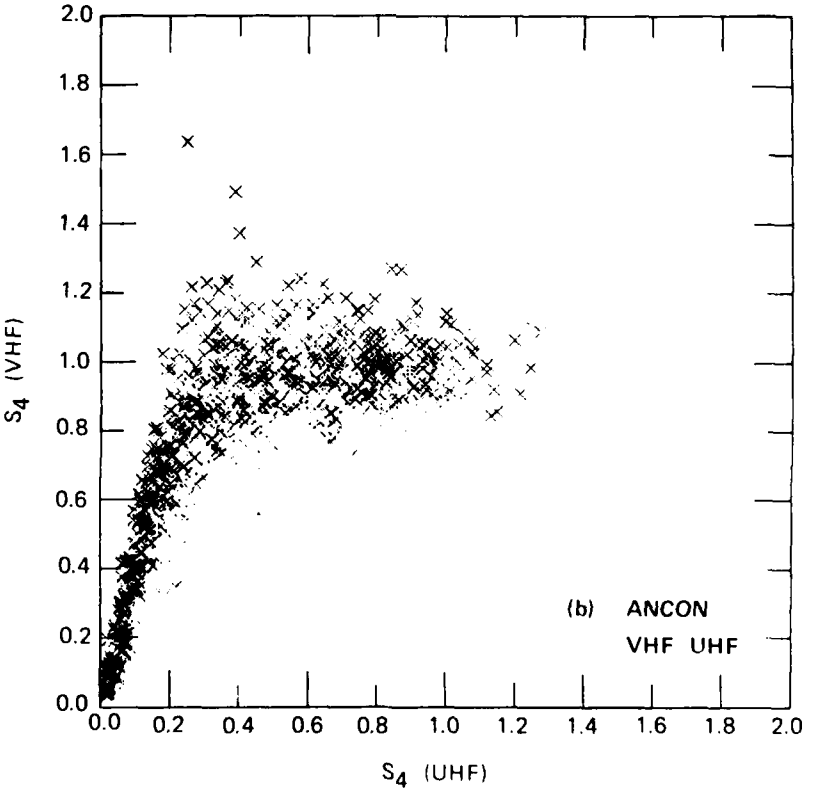

FIGURE 8 SCATTER PLOTS OF S_4 FOR ANCON DATA

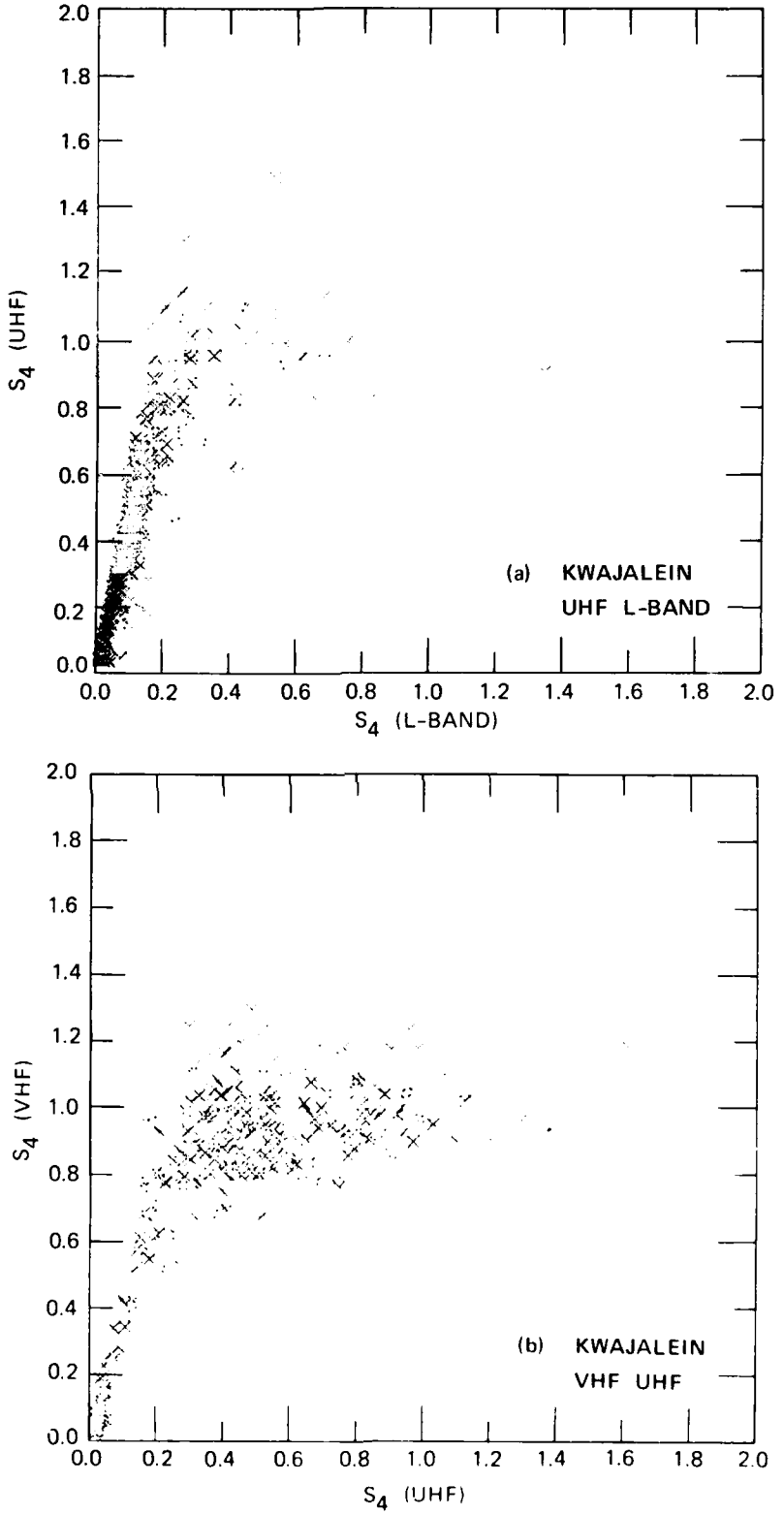

FIGURE 9 SCATTER PLOTS OF S_4 FOR KWAJALEIN DATA

occur unless $p \geq 3$. In any case, these subtleties were suppressed in the standard summary data reported in Rino and Matthews (1978) because of the 10-s detrend filter cutoff.

To summarize, a representative set of disturbed equatorial passes has been processed to obtain both high time and frequency resolution. For small perturbation levels, the first-order phase and amplitude signal moments follow the weak-scatter theory. As the perturbations increase, the rms phase continues to follow the first-order theory, albeit with considerably more scatter. The S_4 values, on the other hand, saturate about a median value of $S_4 = 1$. There is no evidence of strong focusing, which is in agreement with the theory and further confirmation of the shallow p indices.

The structure of the equivalent phase-changing screen is completely characterized by the phase SDF through the T and p parameters. The T parameter combines the effects of absolute turbulent strength, and the conversion of spatial to temporal structure in an anisotropic medium. The diffraction effects are characterized by the Fresnel parameter, Z. Because of the very large extent of the power-law continuum, no significant error is made in neglecting both the inner- and outer-scale spectral cutoffs. That is, these cutoffs are well outside the range of scale sizes that exert a measurable effect on the scintillation.

III THE TEMPORAL STRUCTURE OF INTENSITY SCINTILLATION

To characterize the temporal structure of intensity scintillation, the time delay to 50% decorrelation, τ_I, has been used. Formally,

$$\frac{\langle I(t)I(t + \tau_I)\rangle - 1}{S_4^2} = 0.5 \qquad (17)$$

where it is understood that $\langle I\rangle = 1$. For some applications, however, it is desirable to have a simpler measure of the fade coherence time. Thus, the reciprocal of the upward (or downward) mean level crossing rate, τ_c, has also been computed.

One expects a simple monotonic relation between τ_I and τ_c, with τ_I generally greater than τ_c. Consider that a series of positive and negative impulses has a very short coherence time, but necessarily a longer time between impulses. To verify this behavior, in Figure 10 scatter plots of τ_c vs τ_I are shown for the Ancon data. The corresponding Kwajalein data are shown in Figure 11. Most of the points follow an essentially linear relation. The dispersion is particularly small for the stronger-scatter cases where the coherence times are small.

There are, however, a large number of data points with $\tau_I \gg \tau_c$. These points are confined to conditions of weaker scatter where the fluctuations about the mean intensity level are comparatively small. To verify this, the Kwajalein data shown in Figure 10 have been replotted (Figure 12) with all data points for which $S_4 \leq 0.8$ removed. The few remaining anomalies are attributed to nonstationarities which invariably occur as the propagation path passes through regions of varying perturbation level.

Now, under conditions of weak scatter, the intensity correlation function is given by the formula

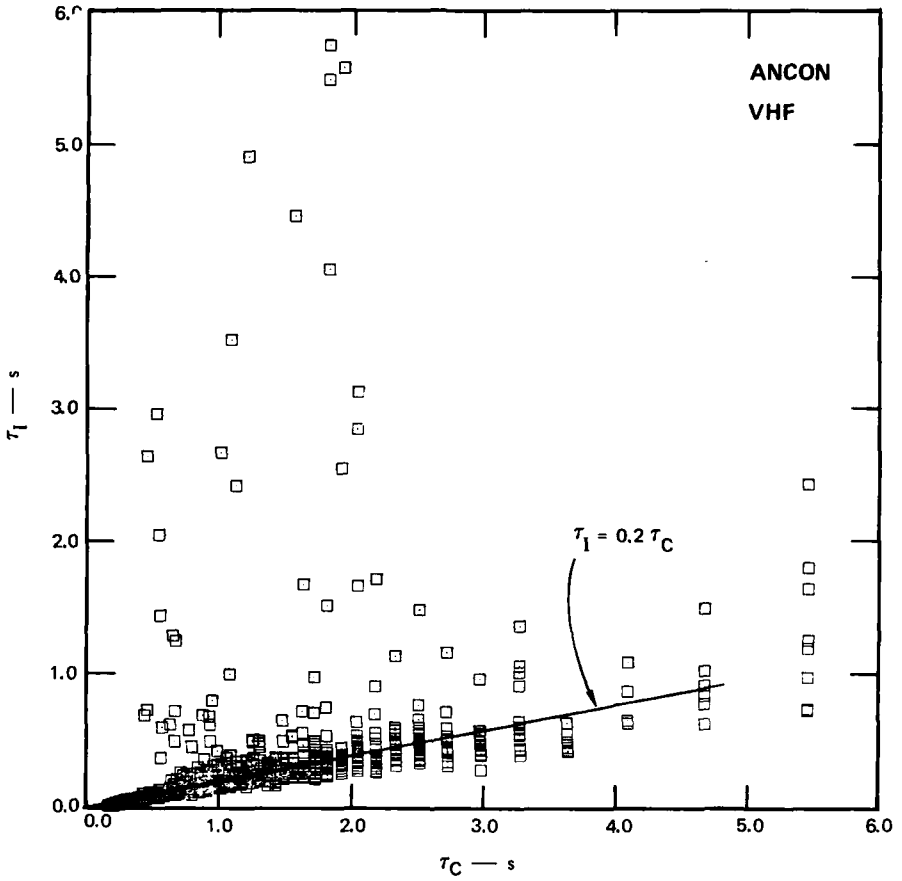

FIGURE 10 SCATTER PLOT OF τ_C vs. τ_I FOR ANCON DATA

$$\langle II' \rangle - 1 = 4r_e^2\lambda^2 \,(L \sec\theta)\, C_s\, Z^{\nu-1/2}$$

$$\times \iint \frac{ab \sin^2(q^2)}{(A'q_x^2 + B'q_y^2 + C'q_y^2)^{\nu+1/2}} \cos\left(\vec{\xi} \cdot \vec{q}\,\frac{\delta t}{\sqrt{2}}\right) \frac{dq_x}{2\pi}\,\frac{dq_y}{2\pi} \,. \quad (18)$$

Equation (18) is a straightforward generalization of Eq. (20) in Rino and Matthews (1978). Indeed, if δt is set equal to zero, Eq. (18) can be evaluated analytically giving the S_4 formula [Eq. (2)] presented in Section I. The vector $\vec{\xi}$ has the units of velocity and it can be derived

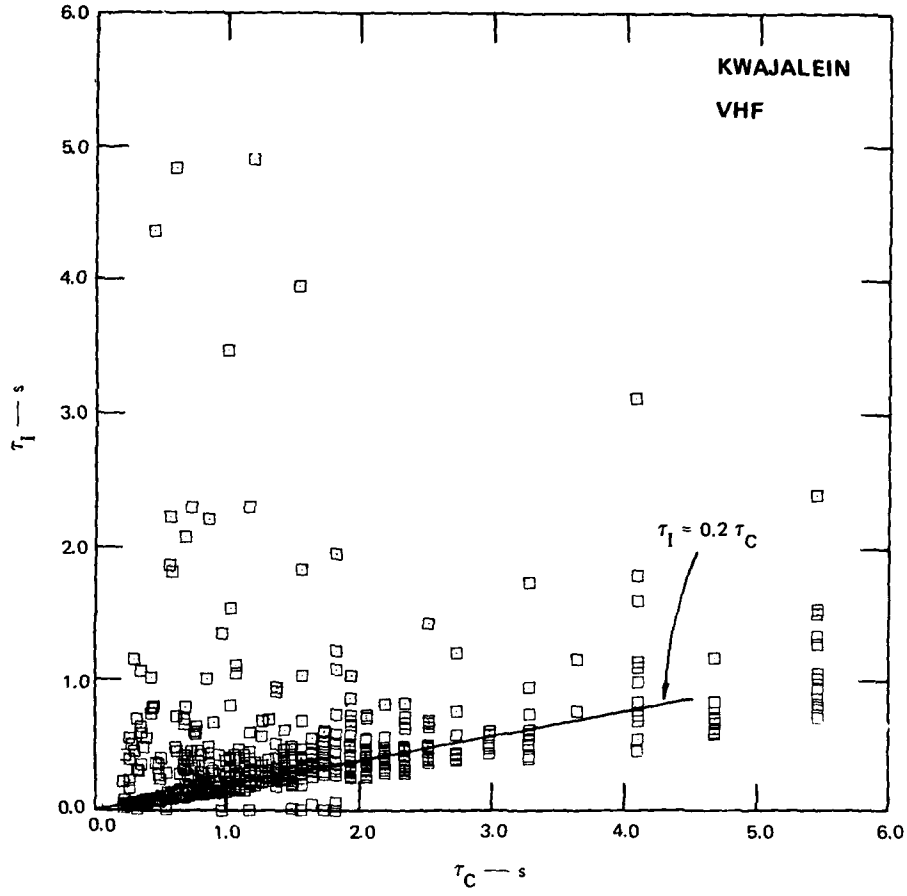

FIGURE 11 SCATTER PLOT OF τ_C vs. τ_I FOR KWAJALEIN DATA

in terms of the actual scan velocity, the propagation geometry, and the irregularity anisotropy (Rino and Livingston, 1978, Section II).

Unfortunately, rather messy numerical integrations would be required to evaluate Eq. (18). Nonetheless, it can be seen that τ_I is independent of perturbation strength. Moreover, one expects τ_I to be a monotomic function of $\sqrt{Z}/v_{eff}$, where v_{eff} is the effective scan velocity discussed in Section I. To verify this dependence, in Figure 13 a scatter diagram of $\log_{10} \tau_I$ vs $\sqrt{Z}/v_{eff}$ is shown.

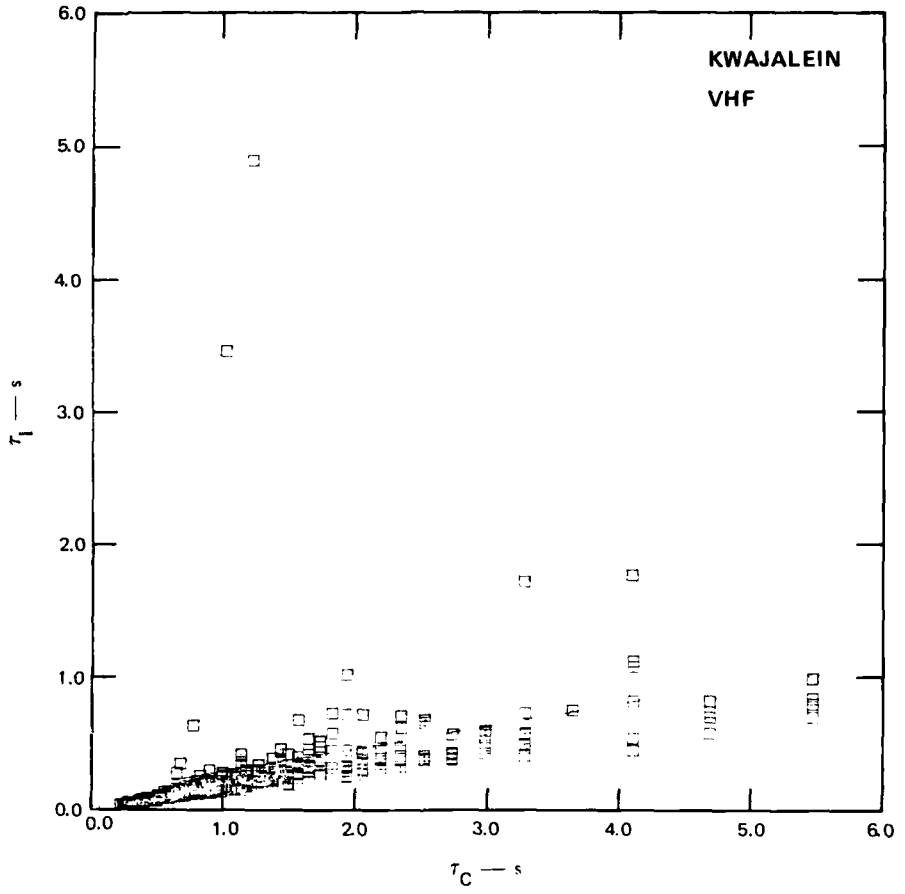

FIGURE 12 REPLOT OF DATA FROM FIGURE 10 WITH DATA POINTS FOR $S_4 \leq 0.8$ REMOVED

The Fresnel radius $\sqrt{\bar{Z}}$ was calculated for a 350-km reference altitude. The effective scan velocity was calculated for 50:1 rod-like irregularities. Superimposed on the scatter diagram is the theoretical curve $\tau_I = K\sqrt{\bar{Z}}/v_{eff}$ for K = 0.16. The value of K, however, is model-dependent. Thus, the best one can do for predictive purposes is to take $\sqrt{\bar{Z}}/v_{eff}$ as an upper bound to the fade coherence time under conditions of weak scatter.

Insofar as the τ_I vs $\sqrt{\bar{Z}}/v_{eff}$ behavior is concerned, the scatter diagrams for Kwajalein and Ancon data show no perceptible difference. Thus, we have shown only the Kwajalein data. On the other hand, if the

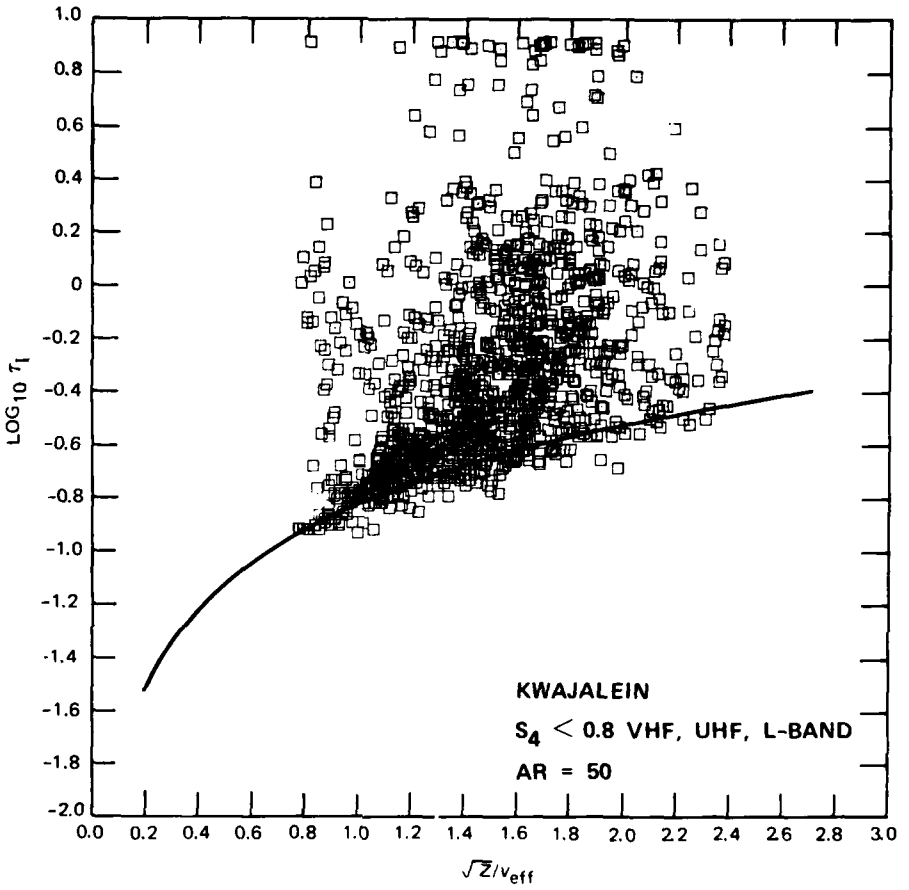

FIGURE 13 SCATTER DIAGRAM OF $LOG_{10}\ \tau_I$ vs. $\sqrt{Z}/v_{eff}$. Superimposed is a plot of $\tau_I = K\sqrt{Z}/v_{eff}$.

τ_I values measured at each frequency are plotted separately, differences between Ancon and Kwajalein data that are consistent with the different spectral slopes do show up.

In Figure 14, τ_I vs S_4 plots are superimposed for the Ancon VHF, UHF, and L-band data. For weak scatter--say, $S_4 \leq 0.4$--τ_I is independent of S_4 but varies monotonically with wavelength because of the dependence on the Fresnel radius. As the perturbation strength increases, the wavelength dependence disappears, giving way to a simple dependence on perturbation strength, as will be shown in more detail shortly. This general behavior, however, is clearly seen in Figure 14.

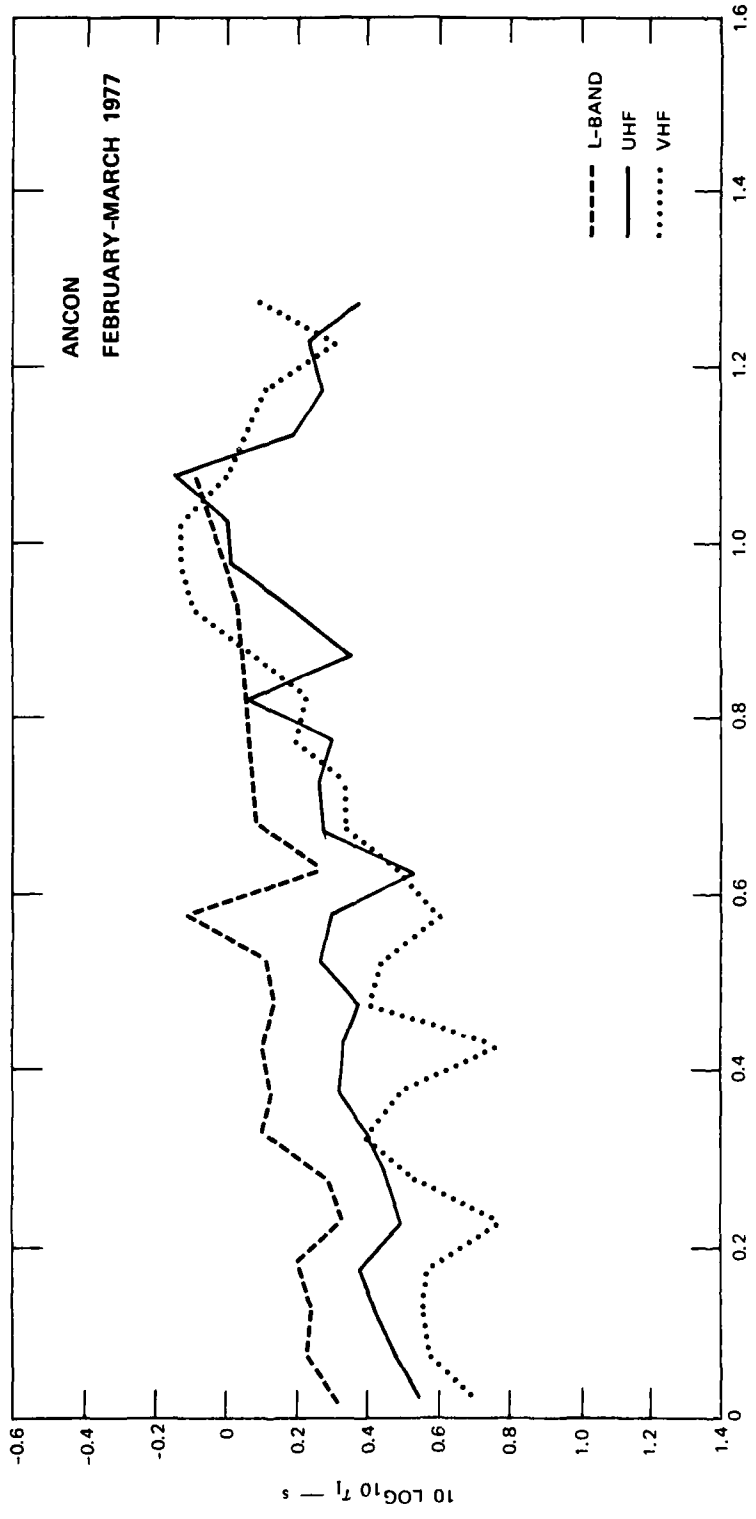

FIGURE 14 SEMI-LOG PLOT OF AVERAGE τ_I VALUES FOR ANCON DATA vs. S_4

The corresponding data for Kwajalein are shown in Figure 15. The general behavior is similar to that of the Ancon data. However, the weak-scatter wavelength dependence is much less pronounced. Indeed, it is virtually lost in the fluctuations of the measurements themselves. This behavior is attributable to the generally flatter phase SDFs observed at Kwajalein, as discussed in Section II.

Let us now consider the intensity coherence time under conditions of strong scattering. Taking Eqs. (12) and (13) as guidelines, it follows that

$$\tau_I = T^{\frac{1}{2\nu-1}} \left[\frac{4\pi^{2\nu-0.5}\,\Gamma(1.5-\nu)}{(2\nu-1)\Gamma(\nu)}\, K \right]^{\frac{1}{2\nu-1}} \tag{19}$$

where

$$K = \log_e \frac{1}{2} \tag{20}$$

for 50% decorrelation. Thus, $\log_{10} \tau_I$ should vary linearly with $\log_{10} T$, with a slope that depends on the spectral slope $\gamma = p/2$.

Thus, in Figures 16 and 17, log-log plots of τ_I vs T are shown for the Ancon and Kwajalein data, respectively. Only points for $S_4 > 0.8$ have been included. The first feature to note in both plots is the very small amount of dispersion in the data for the larger perturbation levels. There is effectively a one-to-one relation between T and τ_I under strong-scatter conditions. Moreover, the relationship follows the power-law form $\tau_I \propto T^{\epsilon}$ with an index $\epsilon = 2\nu - 1$ very close to the value inferred from the measured p indices.

In Figures 16 and 17, theoretical curves based on Eq. (19) are also shown for p = 2.9 and p equal to the index corresponding to the least-squares fit to the respective data sets. It can be seen that the p = 2.9 curves perdict much shorter coherence times for a given T level then are actually observed. The curves corresponding more closely to the measured p indices still predict somewhat smaller coherence times than

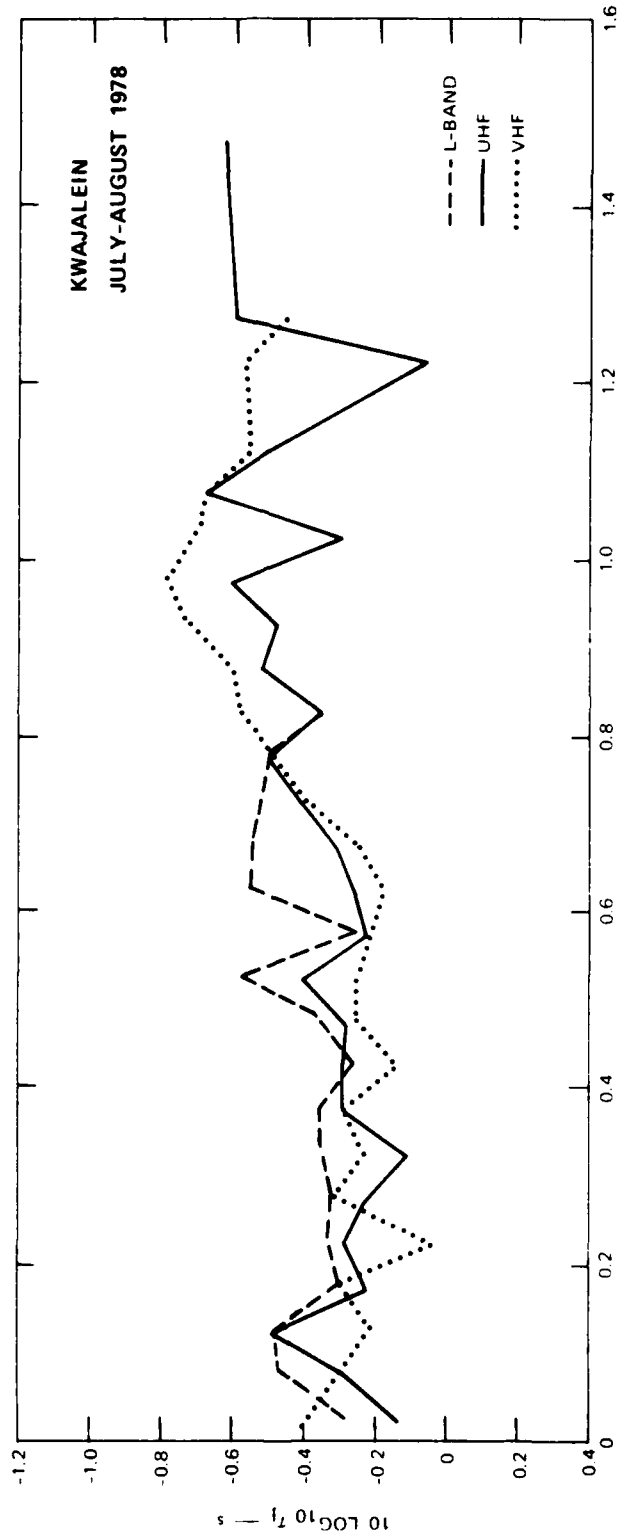

FIGURE 15 SEMI-LOG PLOT OF AVERAGE τ_1 VALUES FOR KWAJALEIN DATA vs. S_4

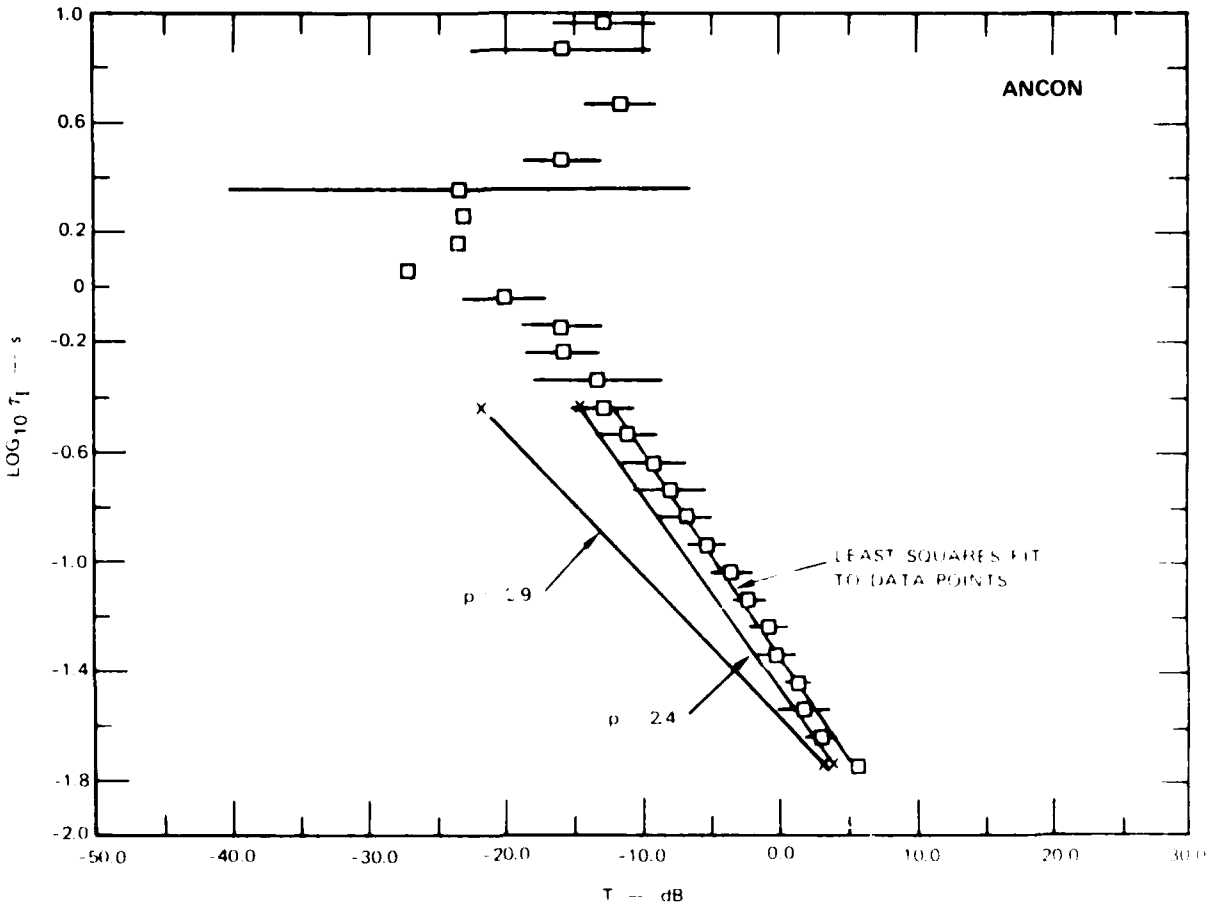

FIGURE 16 LOG-LOG PLOT OF τ_I vs. T FOR ANCON DATA TOGETHER WITH LEAST-SQUARES FIT TO DATA AND THEORETICAL CURVES DERIVED FROM Eq. (19)

are actually observed. Moreover, the differences between Ancon and Kwajalein as far as the inferred p index values are very small.

These small variances between the theory and the data are attributable to the fact that Eq. (19) is an asymptotic result that applies strictly only in the limit as the perturbation becomes arbitrarily large. Moreover, the convergence depends on the spectral index, with the smaller indices converging more slowly. Overall, the internal consistency of the data and its agreement with the theory are very good indeed.

To summarize the practical ramifications of this section, we have demonstrated two bounds for τ_I. Under conditions of weak scattering

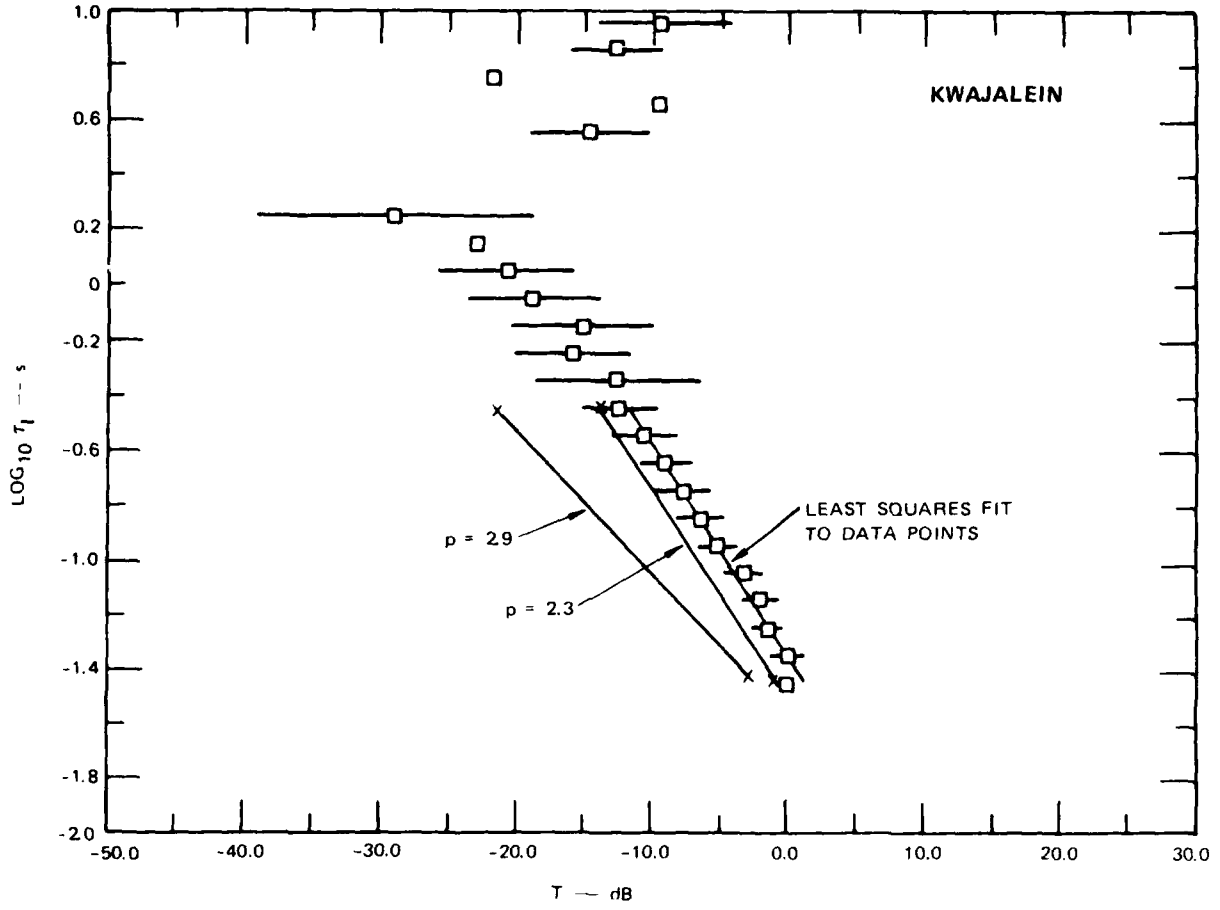

FIGURE 17 LOG-LOG PLOT OF τ_I vs. T FOR KWAJALEIN DATA TOGETHER WITH LEAST-SQUARES FIT TO DATA AND THEORETICAL CURVES DERIVED FROM Eq. (19)

τ_I is independent of perturbation strength and bounded from above by $\sqrt{Z}/v_{eff}$. This bound, however, is rather crude. Under conditions of strong scattering a much tighter lower bound on τ_I is given by Eq. (19). Thus, for predictive purposes it is reasonable to take

$$\tau_I = \min \left\{ \sqrt{Z}/v_{eff},\ T^{\frac{1}{2\nu-1}} \left[\frac{4\pi^{2\nu-0.5}\,\Gamma(1.5-\nu)}{(2\nu\ 0\ 1)\,\Gamma(\nu)}\, K \right]^{\frac{1}{2\nu-1}} \right\} \qquad (21)$$

Fortunately, a tight bound on τ_I under weak-scatter conditions is largely unnecessary because the system effects are not severe.

IV DISCUSSION

The data analysis presented in this report demonstrates the utility of the phase-screen model for interpreting ionospheric scintillation. The results are particularly significant in light of new theoretical results that extend the theoretical results based on the phase-screen model into the strong-scatter regime. This regime, which was previously thought to be mathematically intractable, has yielded results that reproduce the data much more faithfully than the corresponding weak-scatter results.

Thus, in the weak-scatter regime where the intensity coherence time is controlled by $\sqrt{Z}/v_{eff}$, the data show both a high degree of dispersion and a sensitivity to the precise value of the spectral index that is very difficult to model. By comparison, under strong-scatter conditions only the phase turbulent strength, T, and the spectral index, p, need be known to completely specify the intensity autocorrelation function. Moreover, the formula is a simple one, and it accurately reproduces the measured coherence times.

The broader question of how the phase-screen parameters relate to the actual in-situ irregularity structures deserves some careful consideration. The interpretation of scintillation has been strongly influenced by the work of Dyson et al. (1974) who reported one-dimensional in-situ SDFs with power-law indices somewhat less than, but very near, 2 ($1.84 \pm \sim 0.1$). Most researchers have been content to use the nearest integral value 2 for both theoretical calculations and data interpretation.

Moreover, it is well demonstrated that both the gradient-drift and the Rayleigh-Taylor (gravitational) instability generate steep gradients. If such gradients are idealized by actual discontinuities, then the high-frequency portion of the one-dimensional SDF will certainly have the form K_x^{-2} (Costa and Kelley, 1976).

To illustrate this, consider a collection of randomly distributed rods on a line. If the diameters of the rods, ℓ, are distributed according to the probability law $p(\ell)$, then it is easily shown that the one-dimensional SDF has the form

$$\Phi(K_x) \propto 4 \int_0^\infty p(\ell) \left[\frac{\sin^2 K_x \ell}{K_x^2} \right] = K_x^{-2} \left[1 - 2 \int_0^\infty \cos (2K_x \ell)\, p(\ell)\, d\ell \right] \quad . \qquad (22)$$

For any smooth function $p(\ell)$, the second term will decay more rapidly than K_x^{-2}. Hence, for sufficiently large K_x, $\Phi(K_x) \propto K_x^{-2}$.

On the other hand, one can easily generate a reasonable size distribution that will produce a broad spectral regime with a spectral index between 0 and 2. A more realistic distribution of randomly distributed rods on a plane has been treated by Chesnut (1978) with similar results.

If such a simplified model is indeed valid, the important phenomenology question is, what spatial wavenumbers encompass the K_x^{-2} and the $K_x^{-2+\epsilon}$ regimes? The simplest relationship between the in-situ and phase SDFs (Rino and Matthews, 1978) gives a p index one larger than the spectral index corresponding to the one-dimensional in-situ SDF. Thus, K_x^{-2} corresponds to $p = 3$.

Since the Wideband satellite data have consistently shown p values less than 3 for both the auroral zone and equatorial data, it is tempting to conclude that the spatial wavenumbers that cause scintillation lie in the $K_x^{-2+\epsilon}$ regime. Stated another way, the Wideband data suggest that the K_x^{-2} portion of the in-situ SDF cannot persist below spatial wavenumbers corresponding to $\sim$ 200 m.

However, Wittwer (1978) has pointed out that both actual source variations and geometrical smearing due to the varying magnetic aspect angle along the propagation path can upset the simple relation between p and the one-dimensional in-situ index. Studies are currently underway to assess these effects both by looking at in-situ data and performing theoretical computations. Thus, a definitive link must await the culmination of these efforts.

Nonetheless, the fact that verifiable systematic differences in structure are present in the Ancon and Kwajalein data, which have virtually identical propagation geometries, strongly suggest that the measured spectral indices are genuinely mapping the in-situ irregularity structures. Such issues clearly have important phenomenological ramifications.

REFERENCES

Bramley, E. N., "The Diffraction of Waves by an Irregular Refracting Medium," Proc. Roy. Soc. A., Vol. 225, p. 515, 1954.

Chestnut, W. G., private communication, 1978.

Costa, E. and M. C. Kelley, "Calculations of Equatorial Scintillations at VHF and Gigahertz Frequencies Based on a New Model of the Disturbed Equatorial Ionosphere," Geophys. Res. Lett., Vol. 3, No. 11, p. 677, 1976.

Craft, H. D. and L. H. Westerlund, "Scintillations at 4 and 6 GHz Caused by the Ionosphere," paper presented at AIAA 10th Aerospace Sciences Meeting, San Diego, California, January 1972.

Dyson, P. L., J. P. McClure, and W. B. Hanson, "In Situ Measurements of the Spectral Characteristics of F-Region Ionospheric Irregularities," J. Geophys. Res., Vol. 79, p. 1497, 1974.

Fejer, J. A., "The Diffraction of Waves in Passing Through an Irregular Refracting Medium," Proc. Roy. Soc., Vol. 220 a, p. 455, 1953.

Fremouw, E. J., R. L. Leadabrand, R. C. Livingston, M. D. Cousins, C. L. Rino, B. C. Fair, and R. A. Long, "Early Results from the DNA Wideband Satellite Experiment--Complex-Signal Scintillation," Radio Sci., Vol. 13, p. 167, 1978.

Kelley, M. C., G. Haerendel, H. Kappler, A. Valenzuela, B. B. Balsley, D. A. Carter, W. L. Ecklund, C. W. Carlson, B. Hansler, and R. Torbert, "Evidence for a Rayleigh-Taylor Type Instability and Upwelling of Depleted Density Regions During Equatorial Spread-F," Geophys. Res. Lett., Vol. 3, p. 448, 1976.

Koster, J. R., "Equatorial Scintillation," Planet. Space Sci., Vol. 20, p. 1999, 1972.

Koster, J. R., "Equatorial Studies of the VHF Signal Radiated by Intelsat II, F-3. Ionospheric Scintillation," University of Ghana, Accra, Ghana, AD 681462, 1968.

Livingston, R. C., "Comparative Equatorial Scintillation Morphology--American and Pacific Sectors," Topical Report 3, DNA 4644T, Contract DNA001-77-C-0220, SRI Project 6434, SRI International, Menlo Park, CA, 1978.

Marians, M., "Computed Scintillation Spectra for Strong Turbulence," Radio Sci., Vol. 10, No. 1, p. 115, 1975.

Ossakow, S. L. and P. K. Chaturvedi, "Morphological Studies of Rising Equatorial Spread F. Bubbles," J. Geophys. Res., Vol. 83, p. 2085, 1978.

Ott, E., "Theory of Rayleigh-Taylor Bubbles in the Equatorial Ionosphere," J. Geophys. Res., Vol. 83, p. 2066, 1978.

Rino, C. L., "Scintillation Structure in a Severely Disturbed Scattering Environment," Topical Report 2, Contract DNA001-77-C-0038, SRI Project 5960, SRI International, Menlo Park, CA, 1978.

Rino, C. L. and R. C. Livingston, "A Spaced Receiver Data Analysis Technique for Simultaneously Estimating Anisotropy and Pattern Drifts in Radio Wave Transmission Experiments," Topical Report 4, Contract DNA001-77-C-0220, SRI Project 6434, SRI International, Menlo Park, CA, 1978.

Rino, C. L. and S. J. Matthews, "On the Interpretation of Ionospheric Scintillation Data Using a Power-Law Phase Screen Model--Weak Scatter," Topical Report 2, DNA 4606T, Contract DNA001-77-C-0220, SRI Project 6434, SRI International, Menlo Park, CA, 1978.

Rumsey, V. H., "Scintillations Due to a Concentrated Layer with a Power-Law Turbulence Spectrum," Radio Sci., Vol. 10, p. 107, 1975.

Uhlenbeck, G. E. and L. S. Ornstein, "On the Theory of the Brownian Motion," Physical Review, Vol. 36, p. 823, 1930.

Wittwer, L., private communication, 1978.

Woodman, R. F. and C. La Hoz, "Radar Observations of F Region Equatorial Irregularities," J. Geophys. Res., Vol. 81, p. 5447, 1976.

Appendix

DATA BASE FOR TEMPORAL COHERENCE STUDY

Ancon			Kwajalein		
Pass No.	UT Date (1977)	Time	Pass No.	UT Date (1977)	Time
28-01	2/09	04	26-05	7/07	12
28-06	2/11	04	26-06	7/08	12
28-11	2/18	03	26-18	7/28	12
28-20	3/04	04	26-23	7/31	12
28-36	3/15	04	26-27	8/04	13
28-39	3/16	03	26-29	8/06	12
28-42	3/17	04	26-37	8/12	11
28-47	3/19	03	26-40	8/14	11
28-49	3/20	04	26-41	8/14	13
28-50	3/21	03	26-44	8/16	12
29-01	3/21	05	26-46	8/17	11
29-03	3/22	04	26-47	8/17	13
29-05	3/23	04	27-03	8/20	11
29-07	3/24	03	27-08	8/22	11
29-08	3/24	05	27-11	8/23	12
29-12	3/26	04	27-16	8/25	13
29-18	3/29	03	27-19	8/26	12
29-19	3/29	05	27-23	8/29	12
29-21	3/30	04	27-38	9/07	11
29-23	3/31	04			
29-27	4/06	03			
29-31	4/13	04			
29-33	4/14	04			
29-37	4/20	04			

DISTRIBUTION LIST

DEPARTMENT OF DEFENSE

Assistant Secretary of Defense
Comm., Cmd., Cont. & Intell.
ATTN: Dir. of Intelligence Systems, J. Babcock
ATTN: C3IST&CCS, M. Epstein

Assistant Secretary of Defense
Atomic Energy
ATTN: Executive Assistant

Command & Control Technical Center
ATTN: C-650, G. Jones
ATTN: C-312, R. Mason
3 cy ATTN: C-650, W. Heidig

Defense Advanced Rsch. Proj. Agency
ATTN: TIO

Defense Communications Agency
ATTN: Code 480, F. Dieter
ATTN: Code 101B
ATTN: Code 480
ATTN: Code 810, J. Barna
ATTN: Code 205
ATTN: Code R1033, M. Raffensperger

Defense Communications Engineer Center
ATTN: Code R410, J. McLean
ATTN: Code R410, R. Craighill
ATTN: Code R720, J. Worthington
ATTN: Code R123

Defense Intelligence Agency
ATTN: DC-7D, W. Wittig
ATTN: DT-1B
ATTN: DB-4C, E. O'Farrell
ATTN: DB, A. Wise
ATTN: DT-5
ATTN: HQ-TR, J. Stewart

Defense Nuclear Agency
ATTN: STVL
ATTN: DDST
3 cy ATTN: RAAE
4 cy ATTN: TITL

Defense Technical Information Center
12 cy ATTN: DD

Field Command
Defense Nuclear Agency
ATTN: FCPR

Field Command
Defense Nuclear Agency
Livermore Division
ATTN: FCPRL

Interservice Nuclear Weapons School
ATTN: TTV

Joint Chiefs of Staff
ATTN: J-37
ATTN: J-3, WWMCCS Evaluation Office
ATTN: C3S

DEPARTMENT OF DEFENSE (Continued)

Joint Strat. Tgt. Planning Staff
ATTN: JPST, G. Goetz
ATTN: JLTW-2

National Security Agency
ATTN: R-52, J. Skillman
ATTN: W-32, O. Bartlett
ATTN: B-3, F. Leonard

Undersecretary of Def. for Rsch. & Engrg.
ATTN: Strategic & Space Systems (OS)

WWMCCS System Engineering Org.
ATTN: R. Crawford

DEPARTMENT OF ARMY

Assistant Chief of Staff for Automation & Comm.
Department of the Army
ATTN: DAAC-ZT, P. Kenny

Atmospheric Sciences Laboratory
U.S. Army Electronics R&D Command
ATTN: DELAS-EO, F. Niles

BMD Systems Command
Department of the Army
2 cy ATTN: BMDSC-HW

Deputy Chief of Staff for Ops. & Plans
Department of the Army
ATTN: DAMO-RQC

Electronics Tech. & Devices Lab.
U.S. Army Electronics R&D Command
ATTN: DELET-ER, H. Bomke

Harry Diamond Laboratories
Department of the Army
ATTN: DELHD-N-P, F. Wimenitz
ATTN: DELHD-I-TL, M. Weiner
ATTN: DELHD-N-RB, R. Williams
ATTN: DELHD-N-P

U.S. Army Comm.-Elec. Engrg. Instal. Agency
ATTN: CCC-EMEO, W. Nair
ATTN: CCC-EMEO-PED, G. Lane
ATTN: CCC-CED-CCO, W. Neuendorf

U.S. Army Communications Command
ATTN: CC-OPS-W
ATTN: CC-OPS-WR, H. Wilson

U.S. Army Communications R&D Command
ATTN: DRDCO-COM-RY, W. Kesselman

U.S. Army Foreign Science & Tech. Ctr.
ATTN: DRXST-SD

U.S. Army Materiel Dev. & Readiness Cmd.
ATTN: DRCLDC, J. Bender

U.S. Army Nuclear & Chemical Agency
ATTN: Library

DEPARTMENT OF THE ARMY (Continued)

U.S. Army Satellite Comm. Agency
ATTN: Document Control

U.S. Army TRADOC Systems Analysis Activity
ATTN: ATAA-PL
ATTN: ATAA-TCC, F. Payan, Jr.
ATTN: ATAA-TDC

DEPARTMENT OF THE NAVY

Joint Cruise Missile Project Office
Department of the Navy
ATTN: JCM-G-70

Naval Air Development Center
ATTN: Code 6091, M. Setz

Naval Air Systems Command
ATTN: PMA 271

Naval Electronic Systems Command
ATTN: PME 106-13, T. Griffin
ATTN: PME 117-2013, G. Burnhart
ATTN: PME 117-20
ATTN: PME 117-211, B. Kruger
ATTN: Code 501A
ATTN: PME 106-4, S. Kearney
ATTN: Code 3101, T. Hughes

Naval Intelligence Support Ctr.
ATTN: NISC-50

Naval Ocean Systems Center
ATTN: Code 532, J. Bickel
ATTN: Code 5322, M. Paulson
3 cy ATTN: Code 5324, W. Moler

Naval Research Laboratory
ATTN: Code 6780, S. Ossakow
ATTN: Code 7550, J. Davis
ATTN: Code 7500, B. Wald
ATTN: Code 6700, T. Coffey

Naval Space Surveillance System
ATTN: J. Burton

Naval Surface Weapons Center
ATTN: Code F31

Naval Surface Weapons Center
ATTN: Code F-14, R. Butler

Naval Telecommunications Command
ATTN: Code 341

Office of Naval Research
ATTN: Code 420
ATTN: Code 421

Office of the Chief of Naval Operations
ATTN: OP 604C
ATTN: OP 981N
ATTN: OP 941D

Strategic Systems Project Office
Department of the Navy
ATTN: NSP-2722, F. Wimberly
ATTN: NSP-43, Technical Library
ATTN: NSP-2141

DEPARTMENT OF THE AIR FORCE

Aerospace Defense Command
Department of the Air Force
ATTN: DC, T. Long

Air Force Avionics Laboratory
ATTN: AAD, W. Hunt
ATTN: AAD, A. Johnson

Air Force Geophysics Laboratory
ATTN: OPR-1, J. Ulwick
ATTN: PHI, J. Buchau
ATTN: LKB, K. Champion
ATTN: OPR, A. Stair
ATTN: PHP, J. Aarons
ATTN: PHP, J. Mullen

Air Force Weapons Laboratory
ATTN: DYC
ATTN: SUL

Air Logistics Command
Department of the Air Force
ATTN: OO-ALC/MM, R. Blackburn

Assistant Chief of Staff
Intelligence
Department of the Air Force
ATTN: INED

Assistant Chief of Staff
Studies & Analyses
Department of the Air Force
ATTN: AF/SASC, W. Adams
ATTN: AF/SASC, G. Zank

Ballistic Missile Office
Air Force Systems Command
ATTN: MNNH
ATTN: MNNL, S. Kennedy
ATTN: MNNH, M. Baran

Deputy Chief of Staff
Operations Plans and Readiness
Department of the Air Force
ATTN: AFXOXFD
ATTN: AFXOKT
ATTN: AFXOKS
ATTN: AFXOKCD

Deputy Chief of Staff
Research, Development, & Acq.
Department of the Air Force
ATTN: AFRDSS
ATTN: AFRDSP
ATTN: AFRDQ
ATTN: AFRDS

Electronic Systems Division
Department of the Air Force
ATTN: DCKC, J. Clark

Electronic Systems Division
Department of the Air Force
ATTN: XRW, J. Deas

Electronic Systems Division
Department of the Air Force
ATTN: YSEA
ATTN: YSM, J. Kobelski

DEPARTMENT OF THE AIR FORCE (Continued)

Foreign Technology Division
Air Force Systems Command
ATTN: TQTD, B. Ballard
ATTN: NIIS, Library
ATTN: SDEC, A. Oakes

Headquarters Space Division
Air Force Systems Command
ATTN: SKA, M. Clavin
ATTN: SKA, C. Rightmyer

Headquarters Space Division
Air Force Systems Command
ATTN: SZJ, W. Mercer
ATTN: SZJ, L. Doan

Rome Air Development Center
Air Force Systems Command
ATTN: TSLD
ATTN: OCS, V. Coyne

Rome Air Development Center
Air Force Systems Command
ATTN: EEP

Strategic Air Command
Department of the Air Force
ATTN: DCXT
ATTN: OOKSN
ATTN: DCXF
ATTN: XPFS
ATTN: NRT
ATTN: DCXT, T. Jorgensen
ATTN: DCX

OTHER GOVERNMENT AGENCIES

Central Intelligence Agency
ATTN: OSI/PSTD

Department of Commerce
National Bureau of Standards
ATTN: Sec. Officer for R. Moore

Department of Commerce
National Oceanic & Atmospheric Admin.
Environmental Research Laboratories
ATTN: R. Grubb

Institute for Telecommunications Sciences
National Telecommunications & Info. Admin.
ATTN: D. Crombie
ATTN: A. Jean
ATTN: W. Utlaut
ATTN: L. Berry

U.S. Coast Guard
Department of Transportation
ATTN: G-DOE-3/TP54, B. Romine

DEPARTMENT OF ENERGY CONTRACTORS

EG&G, Inc.
ATTN: Document Control for D. Wright
ATTN: Document Control for J. Colvin

Lawrence Livermore Laboratory
ATTN: Document Control for Technical Information
Dept. Library

DEPARTMENT OF ENERGY CONTRACTORS (Continued)

Los Alamos Scientific Laboratory
ATTN: Document Control for P. Keaton
ATTN: Document Control for D. Westervelt
ATTN: Document Control for R. Taschek

Sandia Laboratories
Livermore Laboratory
ATTN: Document Control for T. Cook
ATTN: Document Control for B. Murphey

Sandia Laboratories
ATTN: Document Control for D. Dahlgren
ATTN: Document Control for Space Project Div.
ATTN: Document Control for Org. 1250, W. Brown
ATTN: Document Control for D. Thornbrough
ATTN: Document Control for 3141

DEPARTMENT OF DEFENSE CONTRACTORS

Aerospace Corp.
ATTN: I. Garfunkel
ATTN: T. Salmi
ATTN: V. Josephson
ATTN: R. Slaughter
ATTN: D. Olsen
ATTN: F. Morse
ATTN: N. Stockwell
ATTN: S. Bower

University of Alaska
ATTN: Technical Library
ATTN: N. Brown
ATTN: T. Davis

Analytical Systems Engineering Corp.
ATTN: Radio Sciences

Analytical Systems Engineering Corp.
ATTN: Security

Barry Research Communications
ATTN: J. McLaughlin

BDM Corp.
ATTN: L. Jacobs
ATTN: T. Neighbors

Berkeley Research Associates, Inc.
ATTN: J. Workman

Boeing Co.
ATTN: D. Murray
ATTN: G. Hall
ATTN: S. Tashiro
ATTN: J. Kenney

University of California at San Diego
ATTN: H. Booker

Charles Stark Draper Lab., Inc.
ATTN: D. Cox
ATTN: J. Gilmore

Computer Sciences Corp.
ATTN: H. Blank

Comsat Labs.
ATTN: G. Hyde
ATTN: R. Taur

DEPARTMENT OF DEFENSE CONTRACTORS (Continued)

Cornell University
ATTN: D. Farley, Jr.

Electrospace Systems, Inc.
ATTN: H. Logston

ESL, Inc.
ATTN: J. Marshall
ATTN: J. Roberts
ATTN: C. Prettie

Ford Aerospace & Communications Corp.
ATTN: J. Mattingley

General Electric Co.
ATTN: M. Bortner

General Electric Co.
ATTN: S. Lipson
ATTN: A. Steinmayer
ATTN: C. Zierdt

General Electric Co.
ATTN: F. Reibert

General Electric Co.—TEMPO
ATTN: W. Knapp
ATTN: DASIAC
ATTN: T. Stevens
ATTN: D. Chandler
ATTN: M. Stanton

General Electric Tech. Services Co., Inc.
ATTN: G. Millman

General Research Corp.
ATTN: J. Garbarino
ATTN: J. Ise, Jr.

GTE Sylvania, Inc.
ATTN: M. Cross

HSS, Inc.
ATTN: D. Hansen

IBM Corp.
ATTN: F. Ricci

University of Illinois
ATTN: Security Supervisor for K. Yeh

Institute for Defense Analyses
ATTN: J. Bengston
ATTN: E. Bauer
ATTN: J. Aein
ATTN: H. Wolfhard

International Tel. & Telegraph Corp.
ATTN: G. Wetmore
ATTN: Technical Library

JAYCOR
ATTN: S. Goldman

JAYCOR
ATTN: D. Carlos

Kaman Sciences Corp.
ATTN: T. Meagher

DEPARTMENT OF DEFENSE CONTRACTORS (Continued)

Johns Hopkins University
ATTN: Document Librarian
ATTN: T. Potemra
ATTN: B. Wise
ATTN: T. Evans
ATTN: J. Newland
ATTN: P. Komiske

Linkabit Corp.
ATTN: I. Jacobs

Litton Systems, Inc.
ATTN: R. Grasty

Lockheed Missiles & Space Co., Inc.
ATTN: R. Johnson
ATTN: M. Walt
ATTN: W. Imhof

Lockheed Missiles & Space Co., Inc.
ATTN: D. Churchill
ATTN: Dept. 60-12

M.I.T. Lincoln Lab.
ATTN: D. Towle
ATTN: L. Loughlin

McDonnell Douglas Corp.
ATTN: J. Moule
ATTN: N. Harris
ATTN: W. Olson
ATTN: G. Mroz

Mission Research Corp.
ATTN: S. Gutsche
ATTN: D. Sowle
ATTN: R. Bogusch
ATTN: R. Hendrick
ATTN: F. Fajen

Mitre Corp.
ATTN: C. Callahan
ATTN: G. Harding
ATTN: B. Adams
ATTN: A. Kymmel

Mitre Corp.
ATTN: W. Hall
ATTN: M. Horrocks
ATTN: W. Foster

Pacific-Sierra Research Corp.
ATTN: E. Field, Jr.

Pennsylvania State University
ATTN: Ionospheric Research Lab.

Photometrics, Inc.
ATTN: I. Kofsky

Physical Dynamics, Inc.
ATTN: E. Fremouw

R&D Associates
ATTN: B. Yoon
ATTN: L. Delaney

Rand Corp.
ATTN: E. Bedrozian
ATTN: C. Crain

DEPARTMENT OF DEFENSE CONTRACTORS (Continued)

R&D Associates
ATTN: W. Karzas
ATTN: W. Wright, Jr.
ATTN: M. Gantsweg
ATTN: C. MacDonald
ATTN: H. Ory
ATTN: C. Reifinger
ATTN: B. Gabbard
ATTN: R. Lelevier
ATTN: F. Gilmore
ATTN: R. Turco

Riverside Research Institute
ATTN: V. Trapani

Rockwell International Corp.
ATTN: J. Kristof

Santa Fe Corp.
ATTN: E. Ortlieb

Science Applications, Inc.
ATTN: D. Hamlin
ATTN: L. Linson
ATTN: E. Straker
ATTN: J. McDougall
ATTN: D. Sachs
ATTN: C. Smith

Science Applications, Inc.
ATTN: D. Divis

Science Applications, Inc.
ATTN: SZ

DEPARTMENT OF DEFENSE CONTRACTORS (Continued)

SRI International
ATTN: G. Smith
ATTN: W. Chesnut
ATTN: W. Jaye
ATTN: R. Leadabrand
ATTN: G. Price
ATTN: A. Burns
ATTN: M. Baron
ATTN: R. Livingston
ATTN: D. Neilson
ATTN: J. Owen
3 cy ATTN: C. Rino

Teledyne Brown Engineering
ATTN: R. Deliberis

Tri-Com, Inc.
ATTN: D. Murray

TRW Defense & Space Sys. Group
ATTN: R. Plebuch
ATTN: S. Altschuler
ATTN: D. Dee

Utah State University
ATTN: L. Jensen
ATTN: K. Baker

Visidyne, Inc.
ATTN: J. Carpenter